Growth and Characterization of Thin Films of High Performance Microwave Dielectrics

by

You Li

A Thesis Presented in Partial Fulfillment
of the Requirements for the Degree
Master of Science

Approved June 2013 by the
Graduate Supervisory Committee:

Nathan Newman, Chair
Terry Alford
Rakesh Singh

ARIZONA STATE UNIVERSITY

August 2013

ABSTRACT

Microwave dielectrics are widely used to make resonators and filters in telecommunication systems. The production of thin films with high dielectric constant and low loss could potentially enable a marked reduction in the size of devices and systems. However, studies of these materials in thin film form are very sparse.

In this research, experiments were carried out on practical high-performance dielectrics including $ZrTiO_4$-$ZnNb_2O_6$ (ZTZN) and $Ba(Co,Zn)_{1/3}Nb_{2/3}O_3$ (BCZN) with high dielectric constant and low loss tangent. Thin films were deposited by laser ablation on various substrates, with a systematical study of growth conditions like substrate temperature, oxygen pressure and annealing to optimize the film quality, and the compositional, microstructural, optical and electric properties were characterized. The deposited ZTZN films were randomly oriented polycrystalline on Si substrate and textured on MgO substrate with a tetragonal lattice change at elevated temperature. The BCZN films deposited on MgO substrate showed superior film quality relative to that on other substrates, which grow epitaxially with an orientation of (001) // MgO (001) and (100) // MgO (100) when substrate temperature was above 500 ^oC. In-situ annealing at growth temperature in 200 mTorr oxygen pressure was found to enhance the quality of the films, reducing the peak width of the X-ray Diffraction (XRD) rocking curve to 0.53^o and the χ_{min} of channeling Rutherford Backscattering Spectrometry (RBS) to 8.8% when grown at 800^oC. Atomic Force Microscopy (AFM) was used to study the topography and found a monotonic decrease in the surface roughness when the growth temperature increased. Optical absorption and transmission measurements were used to determine the

energy bandgap and the refractive index respectively. A low-frequency dielectric constant of 34 was measured using a planar interdigital measurement structure. The resistivity of the film is ~3×10^{10} Ω·cm at room temperature and has an activation energy of thermal activated current of 0.66 eV.

ACKNOWLEDGMENTS

First and foremost I would like to express my indebtedness and gratitude to Professor Nathan Newman for his valuable guidance and encouragement throughout my M.S. research. It has been my good fortune to be associated with such an excellent advisor during my study at Arizona State University. I would also like to thank Professors Terry Alford and Dr. Rakesh Singh for helping me as my thesis committee.

I feel grateful for all current and former people who belong to the Professor Newman's research group: Dr. Rakesh Singh, Dr. Zhizhong Tang, Dr. Lei Yu, Dr. Brett Strawbridge, Dr. Lingtao Liu, Mr. Richard Hanley, Mr. Mengchu Huang, Mr. Cameron Kopas, Ms. Tiantian Zhang, Ms. Alena Matusevich, Mr. Makram Abd El Qader, Mr. Mahmoud Vahidi, Mr. Shengke Zhang, Mr. Dexuan Wang and Mr. Patrick Murray. Thanks to you all for creating a compassionate and friendly atmosphere around me.

I acknowledge the helps of the use of facility in LeRoy Eyring Center for Solid State Science (LE-CSSS) at ASU. I will especially thank Mr. Barry Wilkens for his training and great technical support on the RBS, and Dr. Emmanuel Soignard for his help and training on the XRD.

Last but not least, I would like to thank my parents for their continuous support during my study substantially and mentally, without whom I couldn't complete this work. I would also thank my girlfriend, Gege Ma, who always encourages me when I have hard times.

TABLE OF CONTENTS

Page

LIST OF TABLES

LIST OF FIGURES

Chapter 1

MOTIVATION AND INTRODUCTION

1.1 Microwave dielectric materials

Microwave is defined as the electromagnetic wave with a frequency in the range of 300 MHz and 300 GHz, which is mostly used in the telecommunication field. The microwave dielectric materials are used to make components like resonators to excite standing wave with certain frequencies for the communication in certain microwave bands.

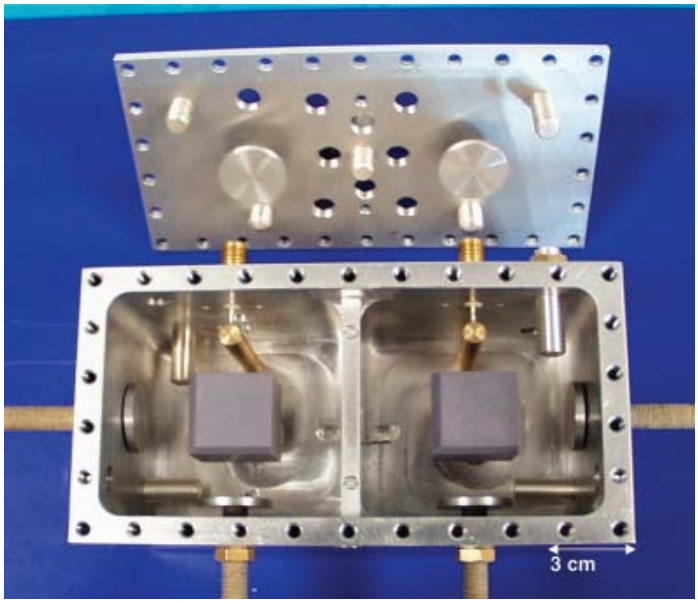

Figure 1.1 Metal cavity with dielectric pucks used in filter and resonator technology [1]

Many kinds of dielectric materials are being used in the microwave communication system, most of which are perovskite based materials with relative high dielectric constant and high quality factor. Here is a table showing the commonly used materials:

Table 1-1 Commonly used dielectric materials [1]

Material	Abbreviation	ε_r	$Q \times f_0$ (GHz)	Structure
$BaMg_{1/3}Ta_{2/3}O_3$	(BMT)	24	250 000	Comp. Per.
$BaZn_{1/3}Ta_{2/3}O_3$	(BZT)	29	150 000	Comp. Per.
$Ba(Co,Zn)_{1/3}Nb_{2/3}O_3$	(BCZN)	34	90 000	Comp. Per.
$SrTiO_3$–$LaAlO_3$	(STLA)	39	60 000	Simp. Per
$CaTiO_3$–$NdAlO_3$	(CTNA)	45	48 000	Simp. Per
$ZrTiO_4$–$ZnNb_2O_6$	(ZTZN)	44	48 000	α pbO_2
$Ba_4Nd_{9.333}Ti_{18}O_{54}$	(BNT)	80	10 000	Per/TTB

Comp., complex; Per, perovskite; Simp., simple; TTB, tetragonal tungsten bronze; MW, microwave.

1.2 Desired properties

There are three parameters of the dielectric materials that we concerned: loss tangent (tanδ), dielectric constant (ε_r) and temperature coefficient of resonant frequency (τ_f).

(1) Loss tangent

Loss tangent (tanδ) shows the dissipation of the energy of the microwave traveling in the materials, which is defined as

$$\tan\delta = \varepsilon'' / \varepsilon' \quad (1\text{-}1)$$

where the ε" and ε' are the imaginary part and real part of the dielectric constant respectively (ε= ε'-iε"). Materials with low tan δ are needed to minimize power dissipation. Often it is expressed in quality factor (Q), the reciprocal of loss tangent:

$$Q = 1/\tan\delta \quad (1\text{-}2)$$

In theory, Q is calculated by the stored energy over the power dissipated in the dielectric and possibly loss to conduction and radiation. It is also measured by the

resonant frequency f_0 over the bandwidth Δf_0 (FWHM) of the resonant peak at 3dB below the maximum height ($Q=f_0/\Delta f_0$). In order to make full use of the available bands, the peak is supposed to be as narrow as possible. For practical purpose, Q should be >30k at 1 GHz [1].

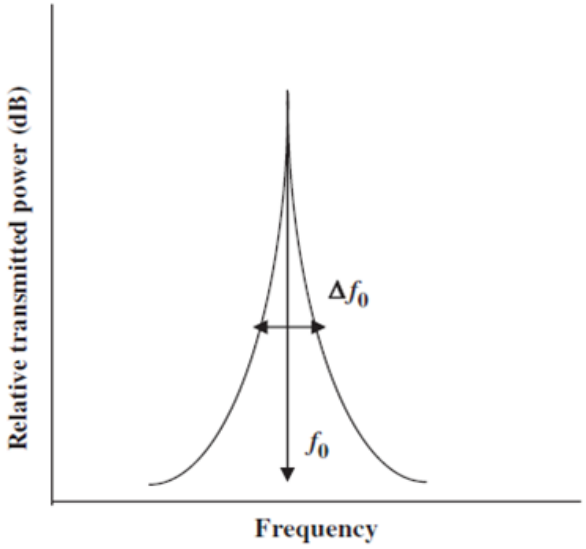

Figure 1.2 Microwave resonant peak of the resonator (f_0 is the resonant frequency, Δf_0 is the bandwidth of the resonant peak at 3 dB below the maximum height) [1]

In theory, the product of Q and f_0 (QF) is a constant, because nearly all the loss mechanism causes higher loss at higher frequency. However, this is not always true. For a given material, the QF product measured at lower frequency at 1-3 GHz is usually smaller than that measured at higher frequency at 5-10 GHz. For perovskite based materials, the QF at 10GHz values can be higher than that at 2GHz by up to a factor of two [2]. Moreover, QF is usually inversely proportional to the dielectric constant, as can be seen in the Table 1-1, which may be due to the different polarizability of the bonds [2].

(2) Dielectric constant (ε_r)

A high dielectric constant ε_r is usually needed to reduce the size of the resonator while maintaining the same resonant frequency, as the resonant frequency f_0 in the resonator can be estimated as [1]

$$f_0=v_p/\lambda=c/\varepsilon^{1/2}/\ \lambda\approx c/\varepsilon^{1/2}/\ D \qquad (1\text{-}3)$$

where v_p is the phase velocity of the microwave, c is the speed of light in vacuum, λ is the wavelength of the standing wave in the resonator, and D is the diameter of the resonator. For a given resonant frequency, D inversely scales as $\varepsilon_r^{1/2}$, thus the size of the resonator can be decreased with a larger ε_r. Due to the volume limit of the component, it is usually required that ε_r >30 [1].

(3) Temperature coefficient of resonant frequency

A near zero temperature coefficient of resonant frequency (τ_f) is important as the resonant frequency must be stable against the temperature change. The τ_f can be expressed in the following relationship [2]:

$$\tau_f = -(\frac{1}{2}\tau_\varepsilon + \alpha_L) \qquad (1\text{-}4)$$

where τ_ε is temperature coefficient of dielectric constant, α_L is the temperature coefficient of linear thermal expansion, all of them are expressed in ppm/^{o}C. τ_f is usually tuned by modifying the composition to ±3 ppm/^{o}C, but sometimes it is also necessary to have a small none zero τ_f to compensate the thermal expansion of the resonant cavity [1].

1.3 Loss mechanisms

There are many potential mechanisms that can lead to the absorption of microwave radiation. Some of them are intrinsic like anharmonic multiphonon processes,

some of them are extrinsic, like unpaired electron spins, polaron, defect, transition metals, and they dominate at different temperature range and doping level [6]. At room temperature it is generally accepted that the dominant intrinsic sources of microwave loss in high performance dielectrics are anharmonic multiphonon processes [18], when the contribution from the extrinsic sources like defects are small. The anharmonic process refers to the transitions between two (or more) phonon modes in order to conserve the total energy and moment. This can explain some features of the change of Q vs. T in some dielectric materials, as can be seen in Fig. 1.3: we measured the Q vs. T relationship of a $ZrTiO_4$ puck down to 4.2 K, the Q increased a lot with decreasing temperature. The lattice becomes more rigid at low temperature, making the vibration of lattice more harmonic, so the anharmonic absorption is suppressed and the loss decreases dramatically.

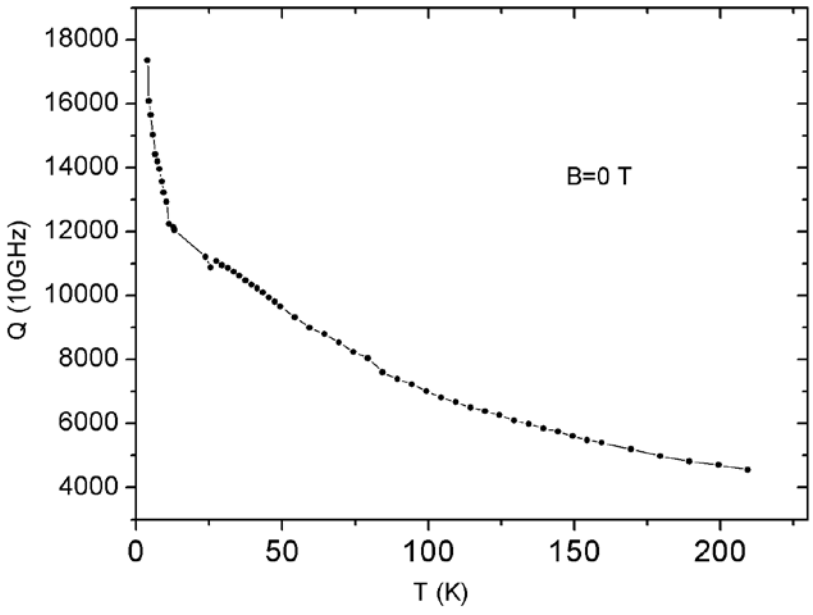

Figure 1.3 Q vs T relationship of a $ZrTiO_4$ bulk measured in a liquid helium dewar with T down to 4.2 K

It has been demonstrated that at cryogenic temperature near 4.2 K, the resonant spin excitations of unpaired transition-metal d electrons in isolated atoms (light doping) or exchange coupled clusters (moderate to high doping) is the dominant loss mechanism [6]. For materials consisting transition metals with unpaired d-shell electrons like Fe, Co, Ni etc., a net magnetic moment will present. When the magnetic field is applied, the energy state of the electron will split into two states as described by Zeeman effect [13]:

$$E=m_s g_e \mu_B B \tag{1-5}$$

where $m_s=\pm 1/2$ is the spin quantum number for electron, g_e is the g-factor (g=2.0023 for free electron), μ_B is the Bohr magneton, and B is the applied magnetic field. The unpaired spin tend to align in the direction of magnetic field which has a lower energy state $E_{parallel}=-1/2 g_e \mu_B B$. It can also absorb energy and flip to a higher energy state $E_{antiparallel}=1/2 g_e \mu_B B$, leading to the microwave loss. Even at zero magnetic field, this mechanism could contributes because of the zero field splitting, and this dominate at cryogenic temperature when the thermal perturbation become less significant [13].

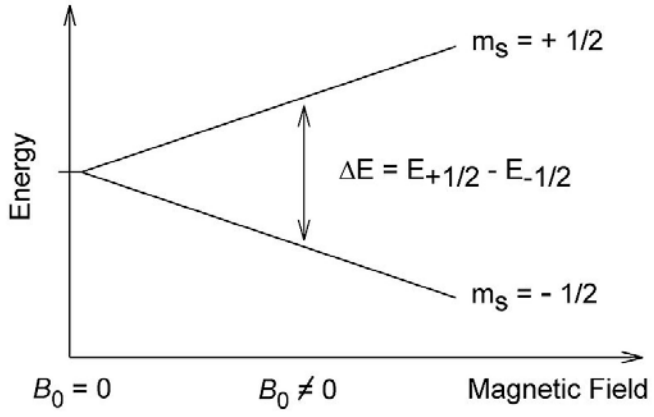

Figure 1.4 The energy state splitting of an electron spin under magnetic field [13]

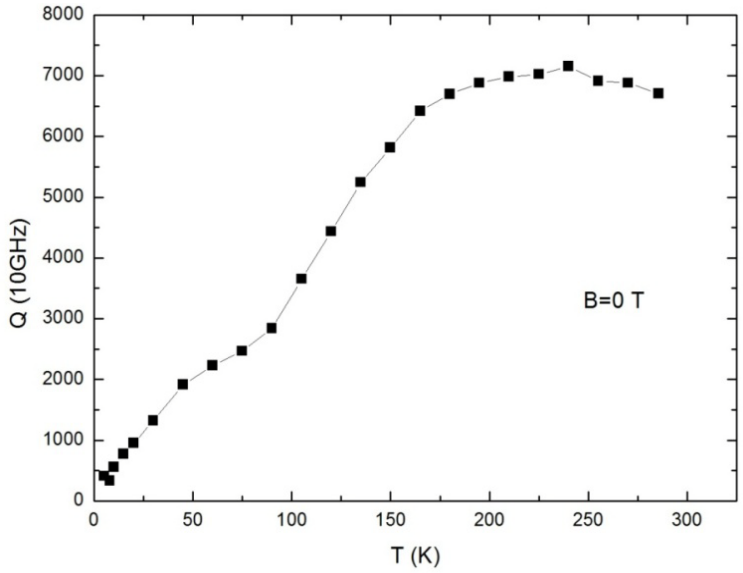

Figure 1.5 Q vs T relationship of a $Ba(Co,Zn)_{1/3}Nb_{2/3}O_3$ bulk measured in a liquid helium dewar with T down to 4.2 K

We measured the Q-T relation of a $Ba(Co,Zn)_{1/3}Nb_{2/3}O_3$ puck as shown in Fig. 1.5. It can be seen that when T decreases, the Q decreases, which is attributed to the Co^{2+} in it. Co^{2+} has d shell electrons arranged as follows:

$$Co^{2+}\ 3d^7 \quad \uparrow\downarrow \ \uparrow\downarrow \ \uparrow \ \uparrow \ \uparrow$$

The three unpaired electron spins can flip and absorb electromagnetic energy, which lead the microwave loss. The loss due to unpaired electron spins can be observed by applying a strong magnetic field. At certain magnetic field, there will be a strong absorption due to the electron spin flip, which is called electron paramagnetic resonances (EPR). The magnetic field is also applied to verify this loss mechanism. It can be seen in Fig. 1.6, there is a significant loss of Q in $Ba(Co,Zn)_{1/3}Nb_{2/3}O_3$ near the 1500 Gauss, which corresponds to the EPR of Co in the material. The broadening of the resonant peak is due to the high doping concentration in the material, which leads to the forming of clusters

[6]. The Q keeps increasing after the resonance with increasing magnetic field, as the energy difference in the two states at high magnetic field are too large for the spin to gain enough energy from the microwave photon to flip, thus the loss decreases, which is consistent with the model.

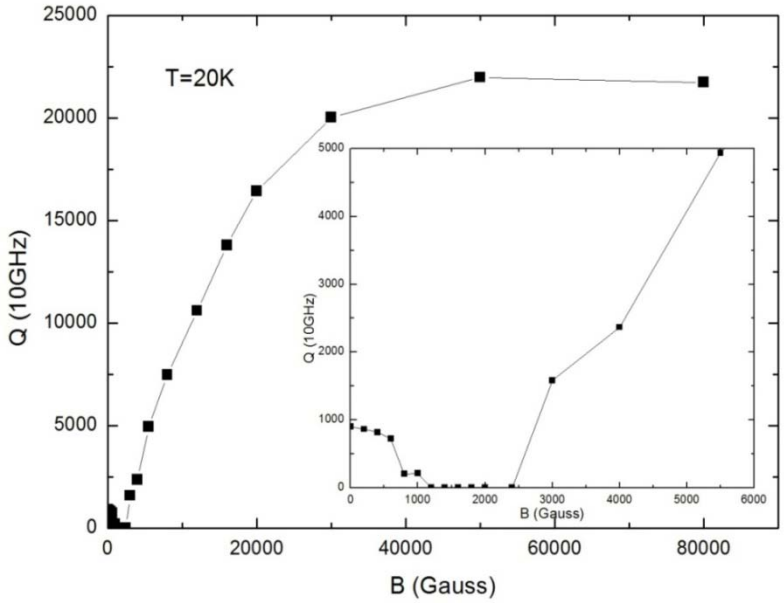

Figure 1.6 The magnetic field dependence of Q of $Ba(Co,Zn)_{1/3}Nb_{2/3}O_3$ bulk measured in a PPMS system keeping the temperature at 20 K, the inset is the zoom-in graph of the drop near 1500 Gauss

The polaron is also considered as a mechanism contributing to the microwave loss. The polaron forms when a free electron or hole is trapped by a cation or anion, which can create unpaired electrons in the atom, which lead to energy level split and thus to loss of microwave.

1.4 Thin films of microwave dielectric materials

The microwave dielectric materials are extensively studied and widely used, but how to grow dielectric thin films with high quality is rarely reported. As it is easier to fabricate perfect thin film than bulk, the study of thin film provides a good approach to study the nature of microwave loss with respect to the microstructure. It is expected that material with better quality should have better dielectric properties. It was reported from the crystallized $(Zr,Sn)TiO_4$ film has a higher dielectric constant (~38) than the amorphous ones (~27) [7], as can be seen in Fig. 1.7. Presumably it is due to the difference in the contribution from the ionic polarization in amorphous and crystallized phase: at around 1 GHz range the major contribution to polarization is ionic and electronic polarization, the crystallized film should have a different atomic potential compared to the amorphous, thus different ionic polarization, as can be seen in the right hand side (b) of Fig 1.8, which can be verified by the infrared phonon measurement.

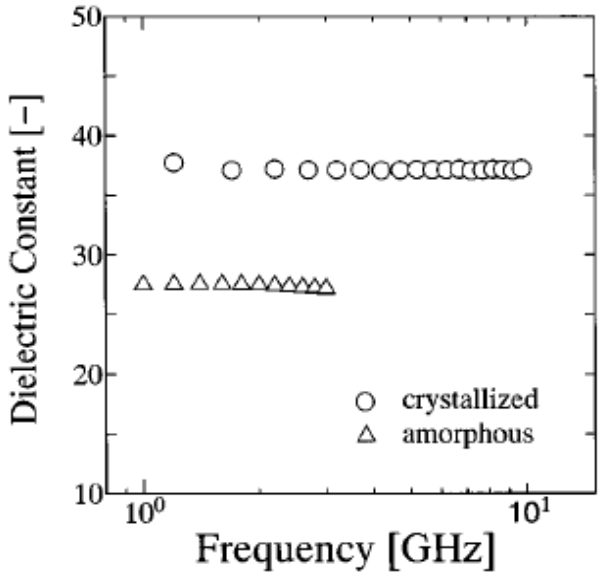

Figure 1.7. The dielectric constant of crystallized and amorphous $(Zr,Sn)TiO_4$ films measured around 1 GHz range [7]

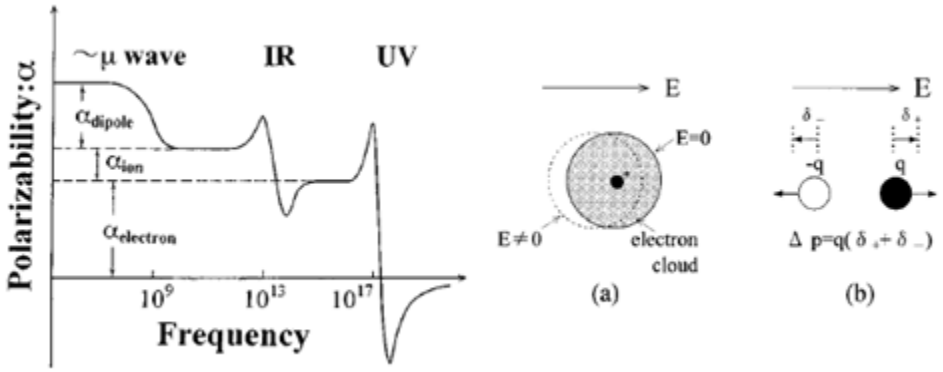

Figure 1.8. (Left) Different mechanisms contributing to the polarization at different frequency range. (Right) (a) Atomic structure showing the electronic polarization. (b) Graph showing the ionic polarization. [7]

Moreover, it is reported that the loss tangent decreased significantly when the film crystallized [8], as can be seen in Fig. 1.9, $ZrTiO_4$ film was grown on Si substrate with RF sputtering. The sharp decrease of the loss tangent of film between 300 ^oC and 400 ^oC is due to a transition from amorphous phase to crystallized phase at 400 ^oC. This is in consistent with the study on the bulk $Ba(Zn_{1/3}Ta_{2/3})O_3$, the ordered structure usually has lower loss tangent [9].

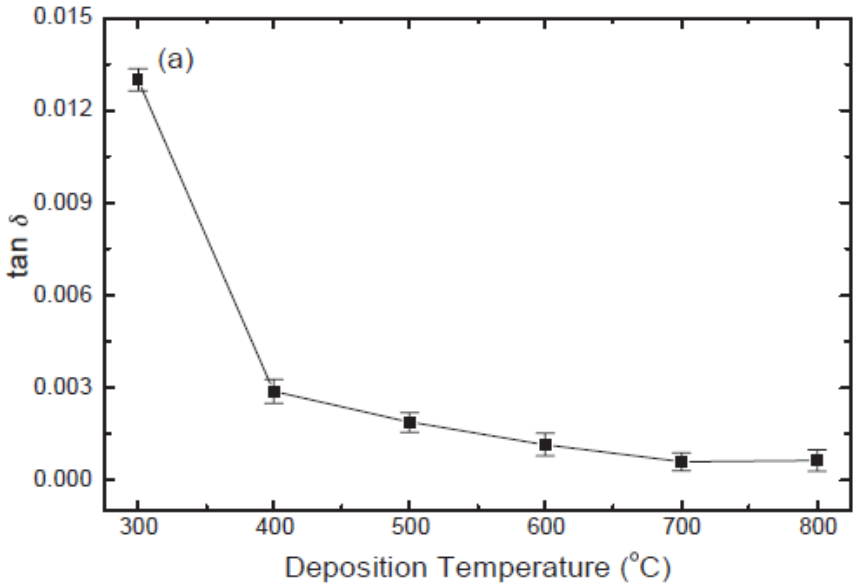

Figure 1.9. The loss tangent of $ZrTiO_4$ film grown on Si at different deposition temperature [8]

In this research, experiments are conducted on practical dielectric materials including $ZrTiO_4$-$ZnNb_2O_6$ (ZTZN) and $Ba(Co,Zn)_{1/3}Nb_{2/3}O_3$ (BCZN). Thin films are fabricated under different conditions to optimize the film quality. Rutherford Backscattering Spectrometry (RBS) and X-Ray Diffraction (XRD) were used to characterize the composition and microstructure. Optical measurements were done to determine the bandgap and refractive index. Planar interdigital structure and Parallel Plate Resonator (PPR) were used to measure the dielectric properties of BCZN films. Efforts are made to find the relation between the microstructure and dielectric properties.

Chapter 2

GROWTH AND CHARACTERIZATION OF $ZrTiO_4$-$ZnNb_2O_6$ THIN FILMS

2.1 Introduction

Zirconium Titanate base material $ZrTiO_4$-$ZnNb_2O_6$ is one of the most widely used dielectric materials in the base station resonator market [1]. $ZrTiO_4$ has an orthorhombic alpha-PbO_2 structure, and can be considered as a solid solution between ZrO_2 and TiO_2. It is reported that when Zr^{4+} is substituted with Sn^{4+}, or Zn^{2+} and Nb^{5+}, a Q of ~40 THz can be obtained, while maintaining a high dielectric constants [2].

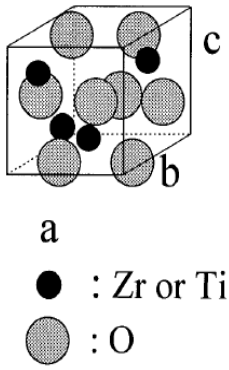

Figure 2.1 Atomic structure of orthorhombic $ZrTiO_4$ [7]

Our sample is a commercial puck (Trans-Tech D4300), 1'' in diameter, 0.25'' in height). As measured from the reflection S_{11} mode in a copper cavity, it has a resonant frequency of 2.27 GHz, unloaded Q_0 of 20072 (QF= 45.54 THz), and a dielectric constant of 42.8, which is higher than the commonly used complex perovskite based materials.

2.2 Pulsed Laser Deposition

The Pulsed Laser Deposition (PLD) technique is employed to grow thin film of ZTZN in this research. PLD is a kind of physical vapor deposition system, where the

evaporation source is a high-power laser situated outside the vacuum deposition chamber so that the high vacuum can be maintained and the chamber can stay clean. As most nonmetallic materials that are evaporated exhibit strong absorption in the ultraviolet spectral range between 200 and 400 nm, the UV laser like KrF eximer is often used. The laser is focus by lens to evaporate the target material and create extremely high temperature in a small region, ablating the target materials and turn it into plasma. Then the evaporated target materials transport and condense on the substrate and form the thin film. Gases like O_2 and Ar are often introduced in the deposition chamber to promote surface reactions, as well as to maintain the stoichiometry of the thin film. Because of the laser pulse's high energy flux and its small absorption length in the target, the PLD process is able to keep the stoichiometric composition of multielement from the target. [9]

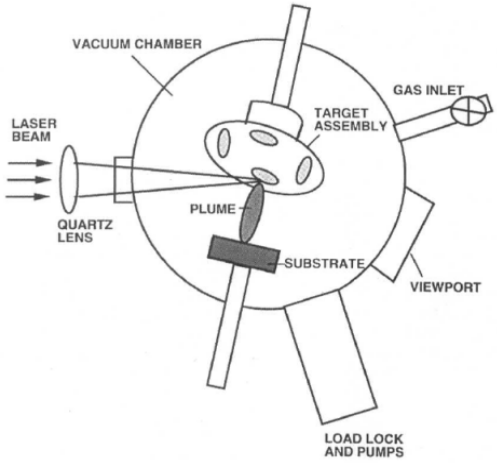

Figure 2.2 Components of a typical PLD system [9]

The process of PLD thin film growth can be generally divided into four stages [11]:

(1) Laser ablation of the target materials which creates the plasma.

(2) The plasma transports to the substrate in highly directional plume.

(3) The ablation materials condense on the substrate.

(4) The condensed materials nucleate and grow on the substrate surface and form the thin film.

The PLD system use in the research is equipped with a KrF excimer laser (Lambda Physik, $\lambda = 248$ nm), with a vacuum chamber which can be pumped down to ~1×10^{-8} Torr.

2.3 Experimental Procedures

The growth of ZTZN film was explored on different substrates including Si (100) and MgO (100). The Si (10mm×10mm×0.525mm, boron doped, p^- type) substrate was ultrasonically cleaned in acetone, ethanol and DI water, and then etched in 5% HF solution for 1 min to remove the surface oxide layer. Then they were ultrasonically cleaned in DI water again, and blew dry with Nitrogen gas. The MgO (100) substrate (10mm×10mm×0.5mm) was cleaned in acetone, ethanol and then blow dry with Nitrogen gas.

After the cleaning, the substrates were stuck to a stainless steel heater using silver paste (Silver Paste Plus, SPI) to achieve a good thermal contact, and baked at 200 ^oC in the oven for 30 min to remove all the organics. Then the heater was loaded into the vacuum chamber of the PLD system. The vacuum chamber was evacuated until the base pressure dropped to ~5×10^{-7} Torr before film growth. The oxygen pressure during growth was kept at 200 mTorr. The laser power was operated at an energy density of 5 $J\cdot cm^{-2}$, and a repetition rate of 5 Hz. The substrate to target distance was ~5 cm. The substrate

temperature varied from room temperature to 750 ^{o}C. Then it was cooled down in the same oxygen pressure in the chamber.

2.3.1 Rutherford Backscattering Spectrometry (RBS)

The composition and thickness of the film is measured by Rutherford Backscattering Spectrometry (RBS). In the RBS measurement, a beam of alpha particles with MeV energy bombasts on to the thin film sample and backscattered by the atoms. The energy of the backscattered alpha particles is related to the Z of the element and the thickness of the film. It can be used to analyze the surface and near surface regions (0-2 microns) of solids. The advantages of non-destructive and requiring no standard to determine the composition to a limit of 0.1% scale make it a perfect method for thin film analysis.

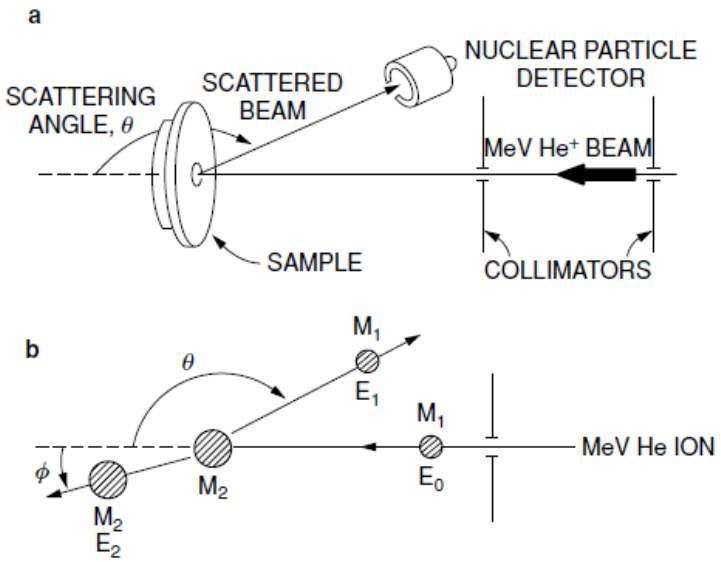

Figure 2.3. Schematic drawing of RBS: a. the geometry of the instrument b. the backscattering process shown by the atoms [12]

A variation of RBS is ion channeling which can locate the lattice locations of impurities or dopants (substitutional vs. interstitial lattice sites). Channeling refers to the influence of the crystal lattice on the trajectories of ions going through the crystal. The atomic rows and planes can be visualized as guides that steer energetic ions along the channels in the crystal lattice. For the atoms situated at the substitutional sites, the yield in channeling RBS will be the same as the host atoms, while for the atoms situated at interstitial sites, as they provide no path for the channeling, the yield will be much higher than the host atoms when the incident beam is aligned in the direction of certain crystalline axis, as shown in Fig. 2.5. [12]

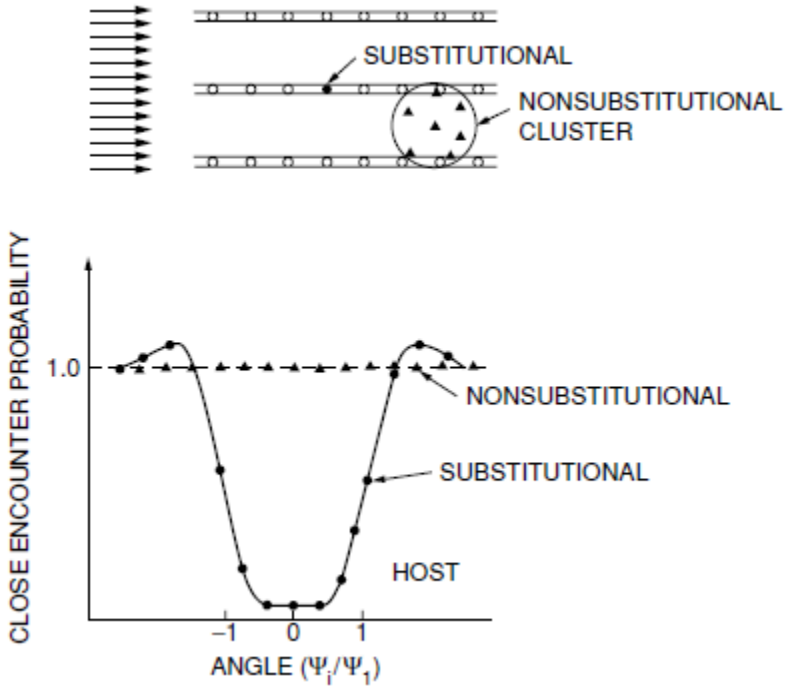

Figure 2.4. (Upper) The substitutional and nonsubstitutional atoms in the channel of the host matrix relative to the incident ion beam. (Bottom) The backscattered yield of the substitutional and nonsubstitutional atoms in the angular distribution scan [12]

The RBS instrument used in the research is a 1.7 MV tandem accelerator located in the CSSS center at ASU, which can accelerate the He ions up to an energy of 5.1MeV. The ion beam is typically 1-2 mm^2 in area. The samples were detected with a 3.05 MeV He^{2+} incident beam. The data analysis was performed using the RUMP software package (Rutherford Backscattering Spectroscopy Analysis Package, Genplot, Cortland, OH).

2.3.2 X-Ray Diffraction (XRD)

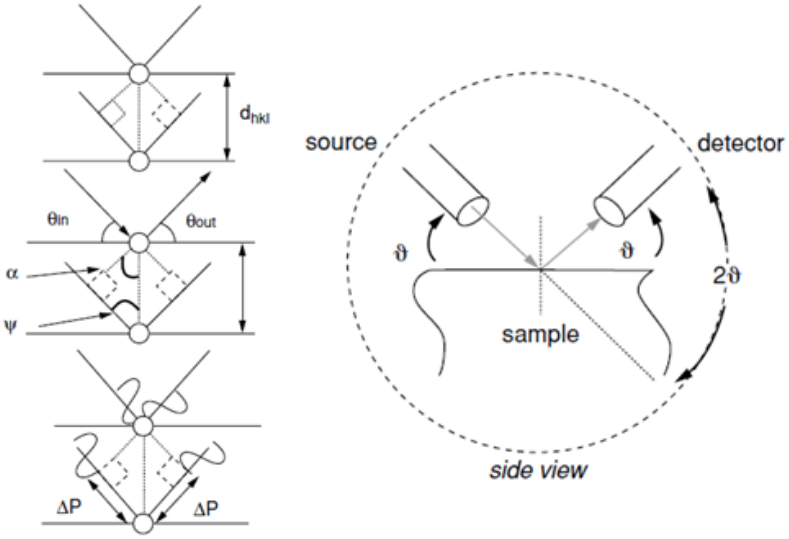

Figure 2.5. (Left) The interference of the reflected X-ray by two adjacent crystalline planes in the material. (Right) The geometry of the diffractometer in θ-2θ scan mode [12]

The phase and microstructure of the film is measure by X-Ray Diffraction (XRD). The film sample is placed at the center of the circle of the diffractometer and detected with the X-ray beam. The X-ray hit the crystalline planes with certain angle θ. Constructive interference happened when the Bragg condition $2d\sin\theta=n\lambda$ is met, and then a strong diffracted beam can be collected with detector at position 2θ. Different phases

with different atoms or crystalline lattice will have different diffraction patterns. XRD can be used to study phase identification and composition, crystal structure, crystal quality, sample texture and so on.

The X-ray diffractometer used in the research is the PANalytical X'Pert Pro MRD using Cu K_α radiations. Manual divergence slit line focus module is used for polycrystalline films. A 19 arc sec hybrid (combination X-ray mirror + channel cut Ge(220) monochromator) line focus module which can remove the $K_{\alpha 2}$ radiation is used for textured film scan. The θ-2θ measurement is carried out in the Bragg-Brentano geometry, to determine the phase and the microstructure. In addition, rocking curve measurement is carried out on the textured film to study the film quality in the normal direction and the distribution of the orientation of the grains. Asymmetric phi scan is carried to check the in-plane film quality.

2.4 Results and discussion

The ZTZN puck material is measured by XRD. The pattern matches the $ZrTiO_4$ phase quite well, and the card number of the reference pattern is 01-080-1783. No $ZnNb_2O_6$ second phase was observed, which indicate that the Zn, Nb atoms are dissolved in the $ZrTiO_4$ matrix and form the solid solution, which is consistent to the literature that they are doped and substituted in the Zr sites, to get better microwave dielectrics properties [2].

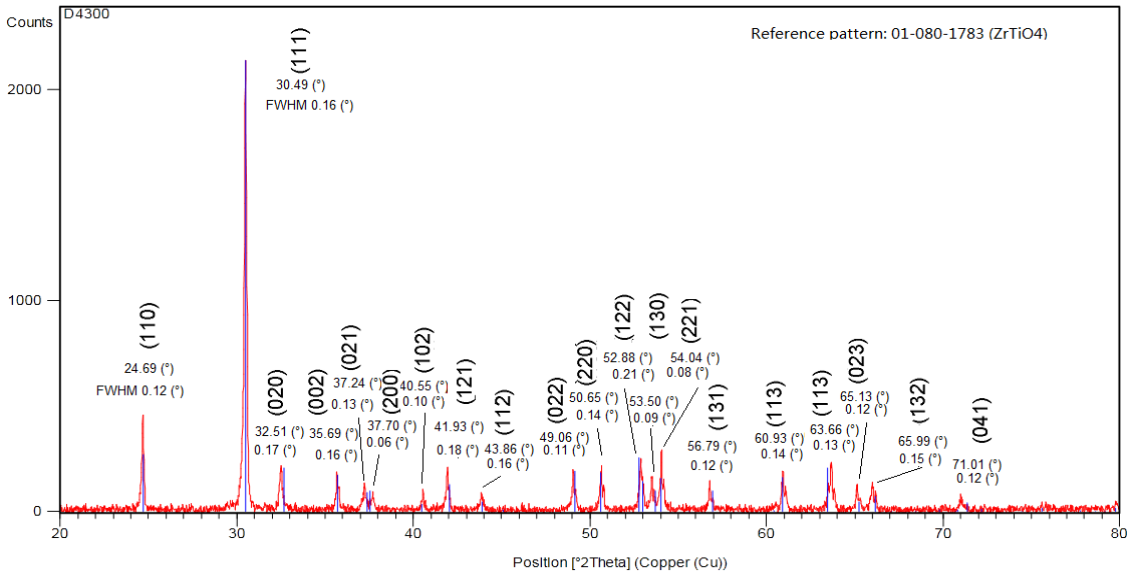

Figure 2.6 The XRD θ-2θ scan of bulk ZTZN

The crystalline lattice calculated from the pattern is orthorhombic with a=4.765 Å, b=5.506 Å, c=5.029 Å, which makes it hard to find a substrate with a good lattice match.

Proton Induced X-ray Emission (PIXE) and Secondary Ion Mass Spectroscopy (SIMS) are used to determine the composition of the bulk material. The composition is determined as $ZrTi_{1.4}Zn_{0.1}Nb_{0.26}O_{5.5}$, with trace amount of Cu, Hf, Mn, Si and Fe.

RBS is used to measure the composition and thickness of the thin film. In order to attain the highest accuracy for the RBS stoichiometry determinations, films were produced with thickness ~100 nm, which results in separate and narrow Zr, Ti, and Zn peaks in the RBS spectra, so the data can be unambiguously and precisely fit. Because the atomic number of Zr and Nb are too close together, the peaks cannot be possibly separated, so the exact ratio between Zr and Nb cannot be determined from RBS measurement. In the simulation, the ratio is inferred from the PIXE result.

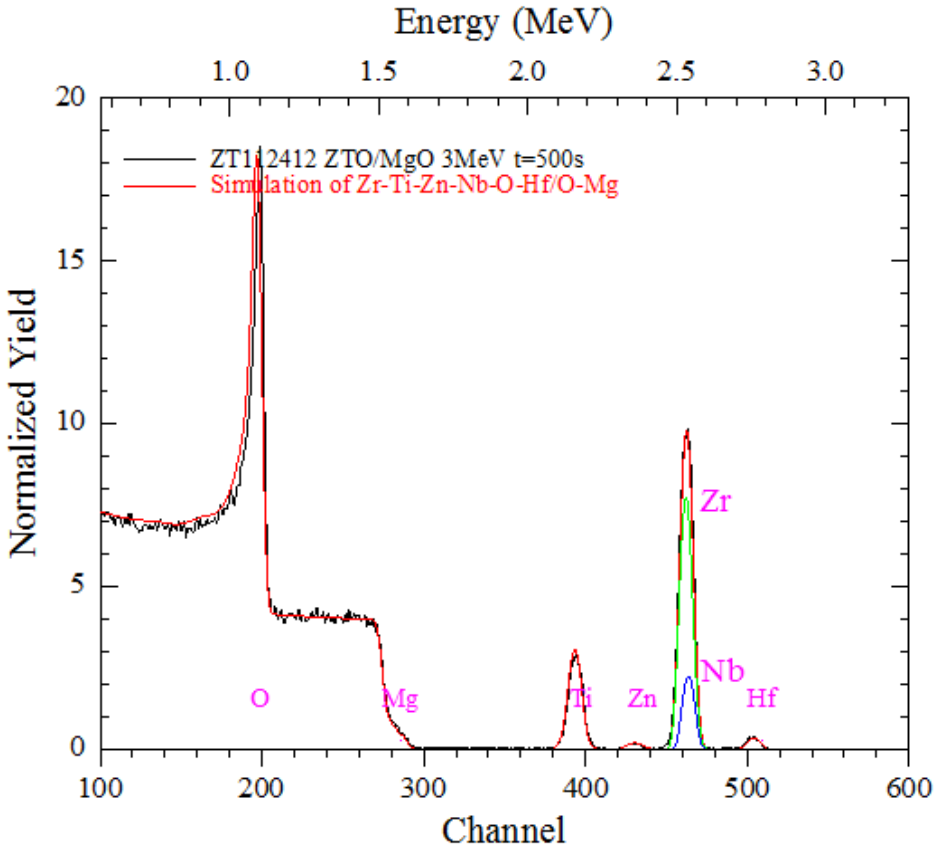

Figure 2.7. RBS spectrum (black) and simulation (red) of a ZTZN thin film sample (on MgO substrate) deposited at 500 ^{o}C

The simulated RBS data of ZTZN on MgO is shown above. The film was grown at 500 ^{o}C, the composition is $ZrTi_{1.4}Zn_{0.05}Nb_{0.26}O_{5.5}$ (and a little Hf as shown in the graph, its amount relative to Zr is about 0.013). Despite the minor Zn loss (as Zn start to sublime at ~400 ^{o}C [14]), this composition was quite similar to that of the bulk. This demonstrates that PLD is a robust method to keep the stoichiometry of complex elements component. The growth rate determined is about 0.6±0.15 Å/pulse.

For all other measurements, film thicknesses in the range of 500±50 nm were used, to study the microstructure of the thin film. A typical RBS spectrum of the film is

shown below, the peak overlapping of different elements renders it impossible to tell the exact composition.

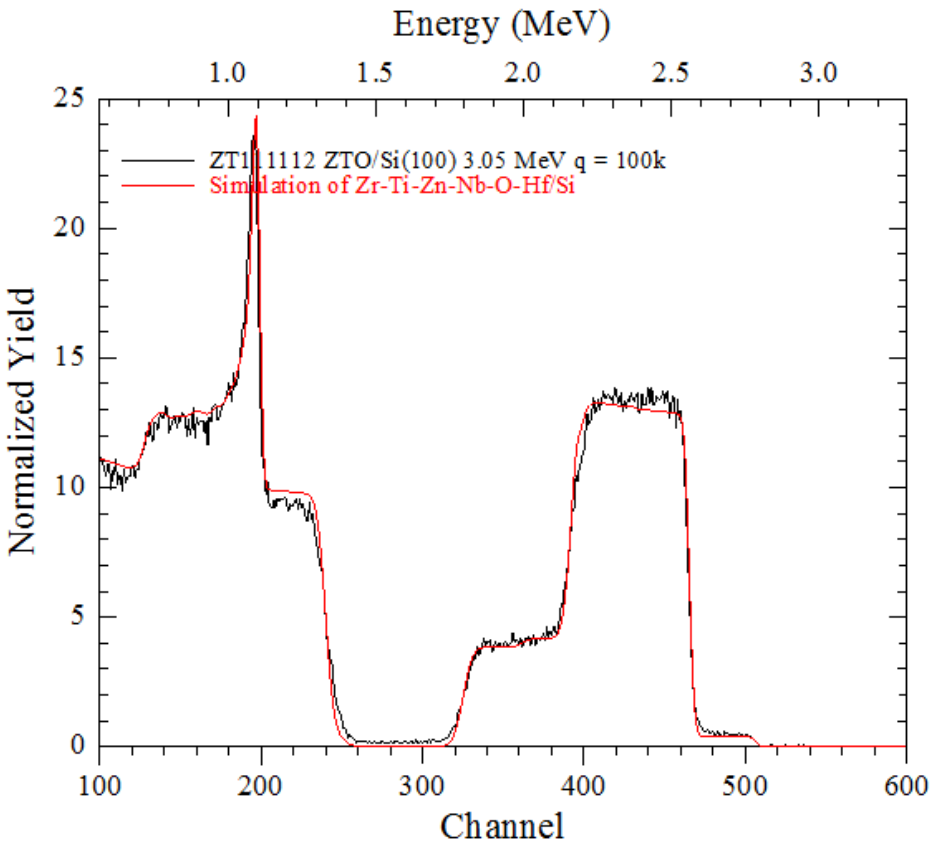

Figure 2.8. RBS spectrum (black) and simulation (red) of a ZTZN thin film sample grown at 700 ^{o}C on Si substrate, the film thickness is determined as 503 nm

The well fit back edge of the backscattered peak indicates that the film is pretty smooth, which is consistent with the topography measurement. The topography is measured by a non-contact optical profilometer (ZeScope) as shown in Fig. 2.9. The film is pretty smooth over the 700 micron range, with $R_a \approx 1.3$ nm.

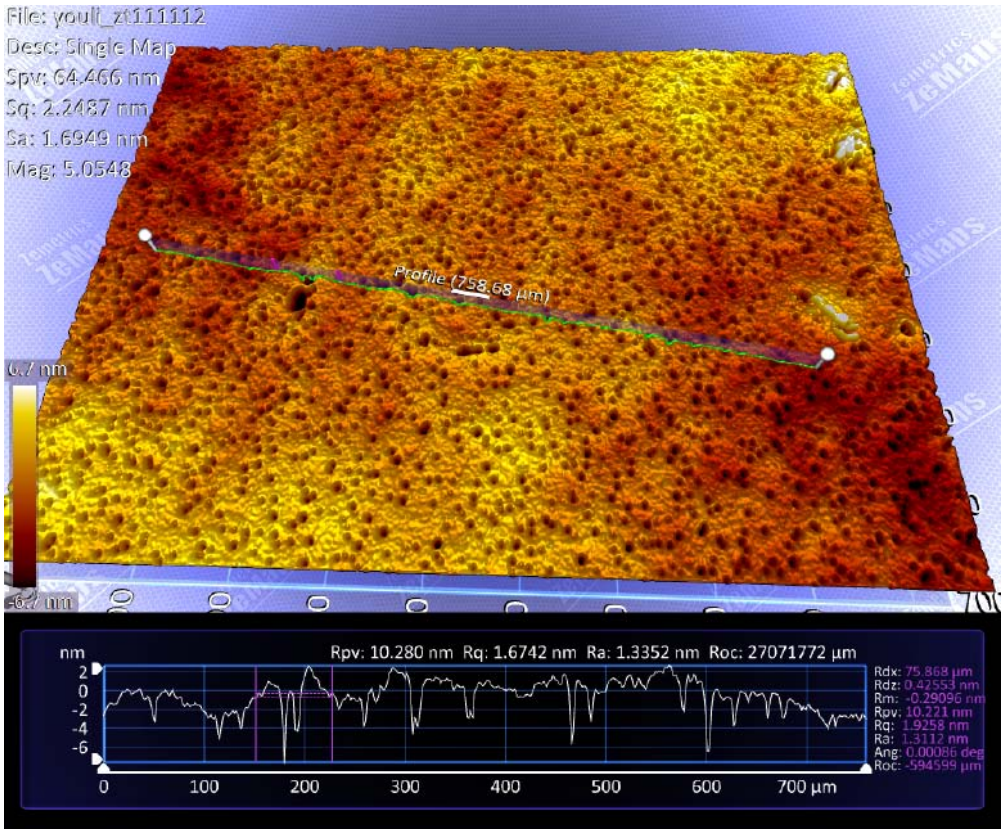

Figure 2.9. The topography of the ZTZN thin film grown on Si substrate at 700^{o}C, measured by a non-contact optical profilometer, the bottom graph shows the roughness.

The films grown on Si from 100^{o}C to 700^{o}C were measured using grazing angle XRD set-up with a fixed sample orientation $\omega=1^{o}$, to facilitate the measurement of the polycrystalline films, thus the peak of substrate Si (001) cannot be seen in the scan.

Fig. 2.10 shows that the film grow on Si is either amorphous or nanocrystalline from 100^{o}C to 500^{o}C. It is slightly crystallized at 600^{o}C, and well crystallized at 700^{o}C. The crystal lattice is determined as a=4.757 Å, b=5.515 Å, c=5.011 Å, which is very close to the bulk (a=4.765 Å, b=5.506 Å, c=5.029 Å). The small difference may be attributed to strain caused by the large lattice mismatch between the film and the Si

(a=5.43 Å) substrates, and the mismatch in a, b and c directions are 11.9%, 0.8%, 7.4% respectively.

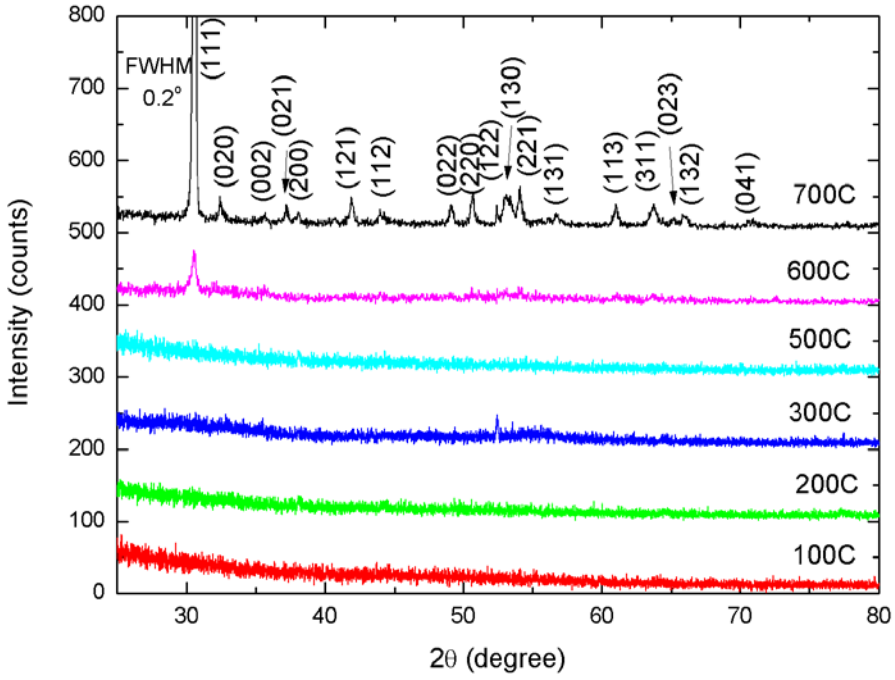

Figure 2.10 XRD grazing angle scan on the ZTZN thin films on Si substrate, grown from room temperature to 700 ^{o}C

For the film grown on MgO at 700 ^{o}C, the film thickness is 530 nm. The film is also very smooth as the back edge of the backscattered peak is well fitted. Despite of the large mismatch between the film and the MgO (a=4.21 Å) substrate, the XRD scan showed that it has a strong texture and grow preferably in (020) direction, which is the same as the substrate MgO (020), shown in the Fig. 2.11.

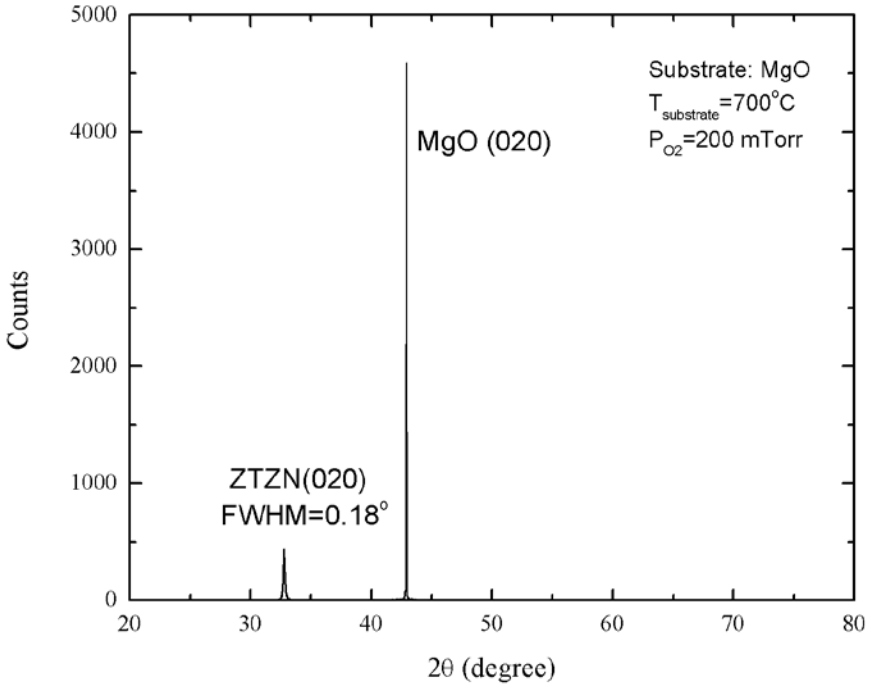

Figure 2.11 XRD θ-2θ scan of ZTZN thin film on MgO grown at 700 °C

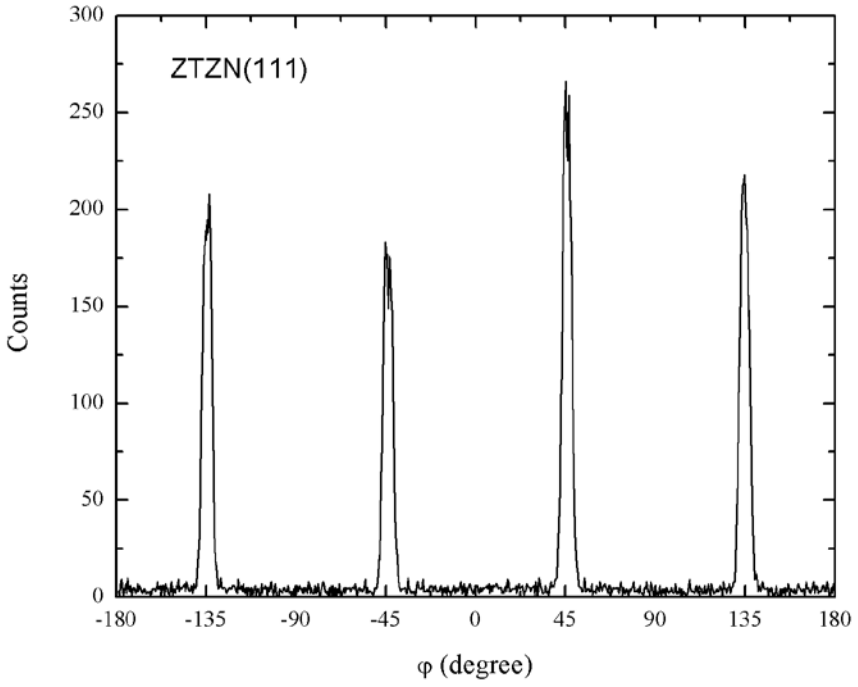

Figure 2.12. XRD asymmetric φ scan of (111) peak of ZTZN thin film

Asymmetric φ scan on ZTZN (111) peak is carried out to check film in-plane alignment as shown in Fig. 2.12. The presence of sharp diffraction peaks every 90^o indicates that it does not contain large-angle grain boundaries. The 4-fold symmetry shows that the film grows along with tetragonal lattice change, which is not observed in the bulk and presumably, presumably due to the stabilization effect from MgO substrate. The lattice constant of the tetragonal phase is determined as a≈4.90 Å and c≈5.46 Å. The lattice constant keeps the same in b direction and increases in a direction and decreases in c direction to conserve the volume of the unit cell. This phenomenon is also reported by other group and explained by domain matching epitaxial growth [15].

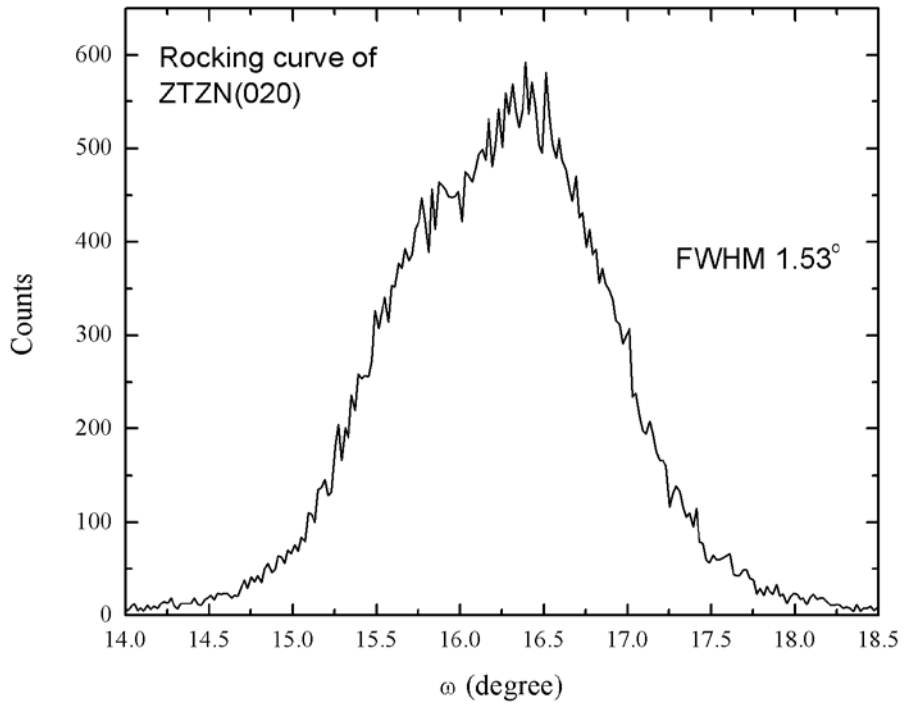

Figure 2.13 XRD rocking curve on the ZTZN thin film (020) peak

The XRD rocking curve on the (020) peak is showed above. The Full Width at Half Maximum (FWHM) of the film is 1.53^o, indicating a lower degree of crystallinity

and a relative wide orientation distribution of the grains, which is expected as there is a large mismatch between the film and the substrate.

Optical absorption measurement is done to characterize the bandgap of the material. For parabolic bands near the band extrema, the relationship between the optical bandgap energy E_g and film absorption coefficient α can be determined using the Tauc plot:

$$(\alpha h\nu)^{1/n}=\beta(h\nu-E_g) \quad (2\text{-}1)$$

where α is the absorption coefficient (≈absorbance divided by sample thickness), β is a constant that depends on material parameters including the effective mass, ν is the frequency of the incident photon, and n is a factor depending on nature of the interband transition near k=0 (n=½ for direct transition, and n=2 for indirect transition) [16]. The optical properties were characterized with a double channel spectrometer (Model DS200, Ocean Optics Inc., Dunedin, FL). An extrapolation of the linear region of the Tauc plot to the energy axis as seen in Fig. 2.15, shows that it is indirect transition with E_g=3.52eV, which is close to the value reported in the literature [15].

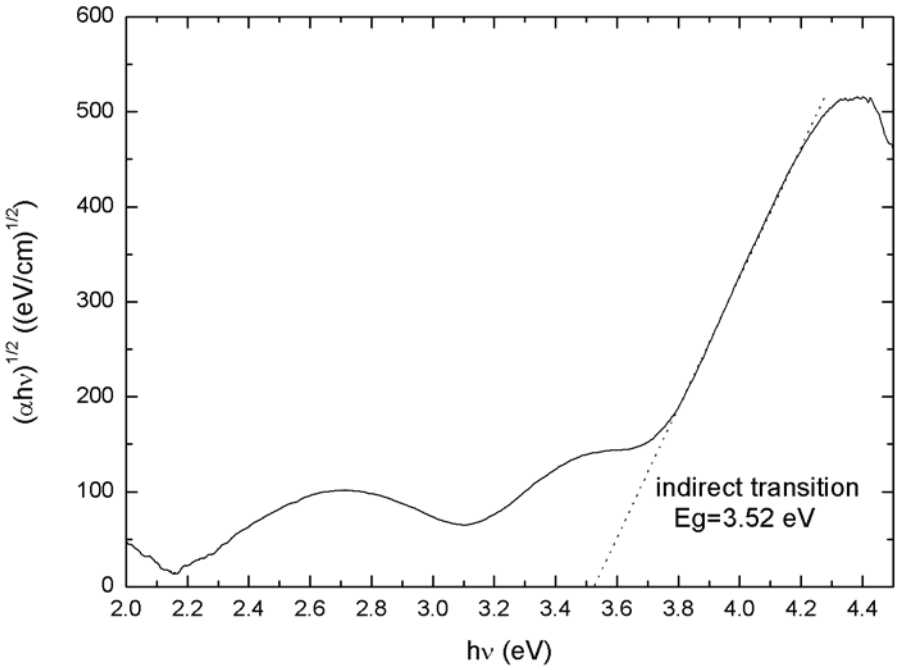

Figure 2.14 Tauc plot for the ZTZN thin film grown on glass at 500 ^{o}C. The straight dashed line pointing at ~3.52 eV is the extrapolation of linear part to the energy axis.

Chapter 3

GROWTH AND CHARACTERIZATION OF EPITAXIAL $Ba(Co,Zn)_{1/3}Nb_{2/3}O_3$ THIN FILMS

3.1 Introduction

Complex perovskite $Ba(B'_{1/3}B''_{2/3})O_3$ dielectrics (where B=Mg, Zn, Co etc. with valence II and B″=Ta, Nb etc. with valence V) are widely used in high-Q resonators and filters for wireless communications. $Ba(Co,Zn)_{1/3}Nb_{2/3}O_3$ (BCZN) is one of the most important in this group, acting as a cheaper replacement for Ta based perovskites like $Ba(Zn_{1/3}Ta_{2/3})O_3$ (BZT) due to the high cost of tantalum ores. It has a high dielectric constant of ~35 and $Q \times f > 90$ THz [1]. It is reported that in the $Ba(X_{1/3}Nb_{2/3})O_3$ system the A site substitution with Sn can further increase the ε_r, but at the expense of Q and τ_f. Only the B site substitution with Co and Zn can tune the τ_f to near zero while maintaining the high Q [3].

The excellent microwave properties as well as the chemical compatibility and similar lattice constant with other commonly used oxides (particularly the perovskites), makes BCZN and related materials appealing candidates for integration in microwave communication and high T_c superconductor oxide thin-film microelectronic devices [19]. Efforts have been made on improving the microwave dielectric properties of the bulk materials [20,21], but studies of these materials in thin film form are sparse. The production of high dielectric constant thin films with low loss and a near-zero τ_f could potentially enable a marked reduction in the size of communication devices and systems. Our previous papers reported the growth of epitaxial and stoichiometric BZT (100) films

[14] and $Ba(Cd_{1/3}Ta_{2/3})O_3$ (BCT) (100) [4] on MgO (100) substrates and the results of structural, chemical, optical and electrical characterizations. One study reported the $Ba(Co_{1/3}Nb_{2/3})O_3$ thin films synthesized on indium tin oxide (ITO) substrates are polycrystalline with far from ideal properties, including a dielectric constant of only ~10 and a surface roughness of over 85 nm [30].

We are not aware of any reports of the growth of BCZN thin films. BCZN has a perovskite lattice structure as shown below, with Ba sitting on the corner (called A site), and Co,Zn and Nb sitting on the body center (called B site). Like other complex perovskites, BCZN can generally have a hexagonal and pseudo-cubic lattice transition caused by the octahedral tilting, but the actual atomic displacements are very small [22]. For simplicity, we used the BCZN pseudo-cubic lattice parameters in this work.

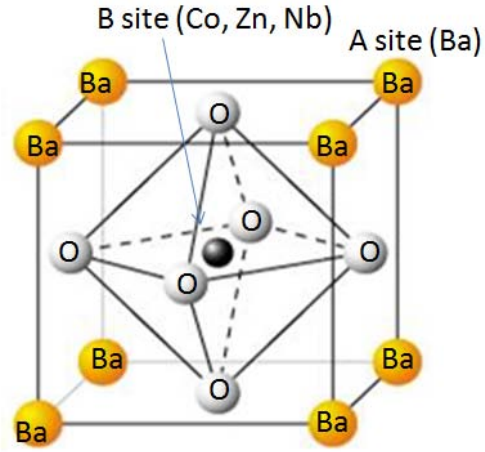

Figure 3.1 The atomic model of BCZN with a complex perovskite structure

Our sample is a commercial puck (Trans-Tech D3500, 1'' in diameter, 0.25'' in height). As we measured from dielectric cavity S_{11} mode, it has a resonant frequency of

2.51 GHz, unloaded Q_0 of 48900 ($Q_0 \times F_L$=123 THz), and a measured dielectric constant of 34.5.

3.2 Experimental Procedures

The growth of BCZN film was explored on different substrates including Si (100), Ge (111), MgO (100), $LaAlO_3$ (100) and Al_2O_3 (0001). The Si (10mm×10mm×0.525mm, p- type) and Ge substrates (10mm×10mm) were ultrasonically cleaned in acetone, ethanol and DI water, then etched in 5% HF solution for 1 min to remove the surface oxide layer. Then they were ultrasonically cleaned in DI water again, and blew dry with Nitrogen gas. The MgO (100) substrate (10mm×10mm×0.5mm) was cleaned in acetone, ethanol and then blow dry with Nitrogen gas. The $LaAlO_3$ (100) and Al_2O_3 (0001) substrate was cleaned in acetone, ethanol and DI water, and then blown dry with Nitrogen gas.

After the cleaning, the substrates were stuck to a stainless steel heater using silver paste (Silver Paste Plus, SPI) to achieve a good thermal contact, and baked at 200 ^{o}C in the oven for 30 min to remove all the organics and form a dense silver network for the thermal conduction. Then the heater was loaded into the vacuum chamber of the PLD system. The vacuum chamber was evacuated until the base pressure dropped to ~5×10^{-7} Torr before film growth. The oxygen pressure during growth was kept at a pressure between 50 and 500 mTorr. The laser power was operated at an energy density of 5 J·cm^{-2}, and a repetition rate of 5 Hz. The substrate to target distance was ~5 cm. The substrate temperature varied from room temperature to 800 ^{o}C. Some of the films were in-situ annealed in the chamber with temperature and oxygen pressure the same as growth condition. Then it was cooled down with the same oxygen pressure in the chamber.

3.3 Result and discussion

The BCZN puck material is measured by XRD. The pattern matches the $Ba(Zn_{1/3}Nb_{2/3})O_3$ phase quite well, and the card number of the reference pattern is 00-039-1474. No peak splitting is observed, presumably indicating no B site ordering formed during the processing. The lattice constant is determined as a= 4.093 Å.

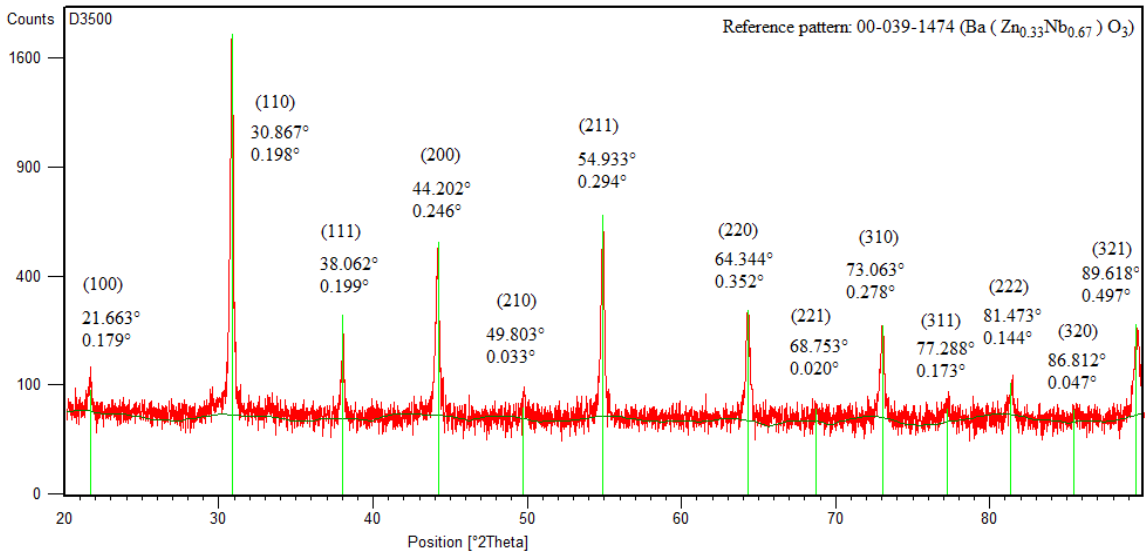

Figure 3.2 XRD θ-2θ scan of the BCZN bulk material

PIXE and SIMS are done to measure the composition of the puck. The composition is determined as $BaCo_{0.23}\,Zn_{0.1}\,Nb_{0.55}\,O_3$, with trace amount of Zr, Mn, Na, Mg and Ca.

The composition of the film was studied at a series of growth temperatures as summarized in Fig. 3.3. Each element's composition was plotted relative to Ba due to the expected unity sticking coefficient of this element. This is assumption is made because of the non-volatile nature of both elemental Ba and its oxides. The Nb:Ba and Co:Ba ratios were found to be ~0.6 and 0.2 respectively, consistent with the target's composition.

This indicates that Nb and Co also have a near-unity sticking coefficient and are readily incorporated into the thin film. The Zn:Ba ratio dropped from 0.05 at room temperature to 0.03 for growth temperatures of 500 ^{o}C and above due to the volatility of Zn. Due to overlap between the oxygen peak from the substrate and the film, the oxygen content in the film could not be accurately determined. The measured thickness inferred that the average growth rate for the depositions was 0.9±0.2 Å/pulse (27±6 nm/min) for the sample located near the center of the substrate holder.

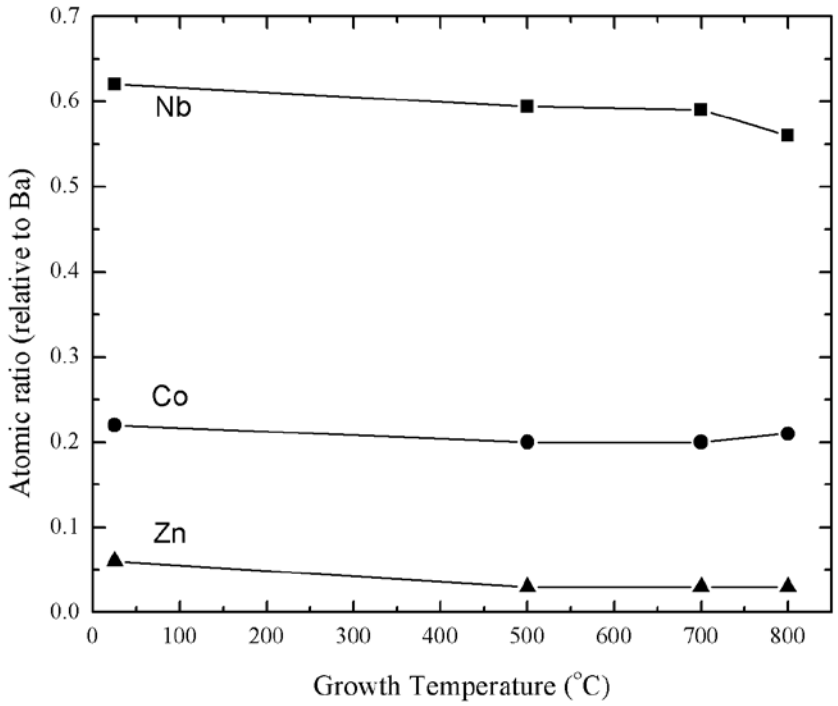

Figure 3.3 The composition of the $Ba(Co,Zn)_{1/3}Nb_{2/3}O_3$ film grown at different temperatures, the atomic ratios of Nb, Co and Zn are shown relative to Ba.

The films with the best quality were grown on the MgO substrate with thickness of 450±50 nm. In general, a high growth temperature is needed to overcome the kinetic barriers required to achieve epitaxial growth of oxide thin films. The results of XRD θ-2θ

scan were summarized in Fig. 3.4. The absence of crystalline peak in the X-ray diffraction data for the film grown at room temperature suggests that the film is amorphous. At 400 ^{o}C the peaks match the diffraction pattern of $Ba(Co_{1/3}Nb_{2/3})O_3$ phase, indicating that the film is polycrystalline. As the temperature was increased above 500^{o}C, the (011) peaks decreased and (00l) peaks increased, indicating enhanced texturing with an alignment of the film (00l) to the substrate MgO(002) in the normal direction. There is no evidence of B-site ordering superlattice peaks in the scan of either the film or the bulk. Asymmetric φ scan on BCZN off-axis (110) plane was carried out to characterize the in-plane alignment. The scan illustrated in Fig. 3.5 was performed on the sample grown at 700 ^{o}C, the BCZN(011) and MgO(022) were measured at corresponding 2θ and ψ angles respectively while keeping φ=0 position and all the other parameters the same. The presence of sharp diffraction peaks every 90^{o} with peak width of 1.5^{o} indicates that it does not contain large-angle grain boundaries. These results indicate an in-plane alignment of BCZN(100)//MgO(100). In order to better understand how the films grow relative to the substrate, as there is a 2.8% lattice mismatch between the bulk (a=4.094 Å) and the MgO substrate (a=4.214 Å), XRD reciprocal space mapping scans were done around the (002) and (202) peaks of the film grown at 700 ^{o}C, using the MgO(002) and (202) peaks as references. The results show that the tilting in the normal direction should be within 0.05^{o}, verifying the good alignment relative to the substrate, The lattice constant was determined to be a=4.097 Å and c=4.083 Å, indicating a tetragonal lattice, which is stretched in plane by the substrate and shrinks in the normal direction to conserve the volume of the unit cell [23].

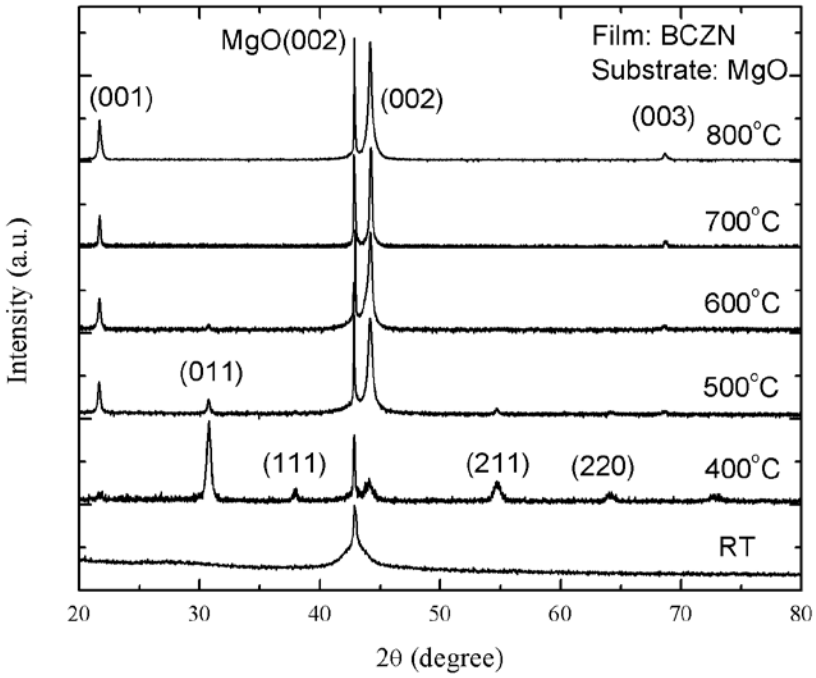

Figure 3.4. XRD θ-2θ scans of BCZN films grown on MgO substrates at different temperatures

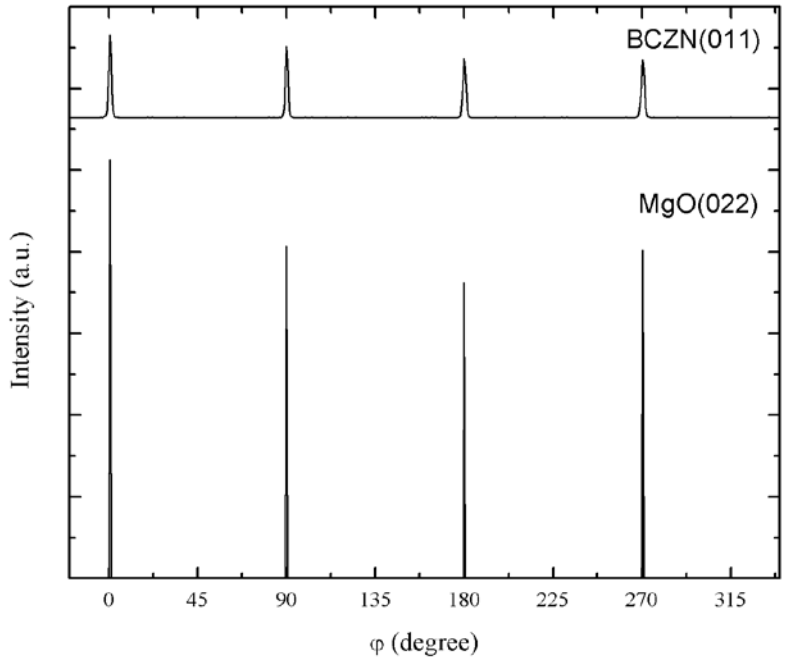

Figure 3.5. XRD asymmetric φ scan of BCZN film on MgO substrate grown at 700 °C.

Different oxygen pressure and heat treatment were used to study the growth conditions to optimize the film quality. Oxygen pressures of 50 and 200 mTorr were studied, the sample grown at 200 mTorr showed the better film quality with smaller FWHM of XRD rocking curve. Enhanced oxygen pressures (a) increase the fraction of non-volatile oxides on the hot growth surface, and (b) reduce the energy of impinging species on the growth surface. Both of these suppress surface diffusion, which inhibits high-quality epitaxy [14]. In-situ annealing was also found to enhance the film quality, as shown by the XRD rocking-curve results of BCZN (002) peaks in Fig. 3.6 for two films grown at 700 ^{o}C. After in-situ annealing at 700 ^{o}C for 30 min, the FWHM decreased from 1.53^{o} to 0.59^{o}, showing significantly improved epitaxy. The film shows a slightly smaller rocking curve of 0.53^{o} wide grown at 800 ^{o}C.

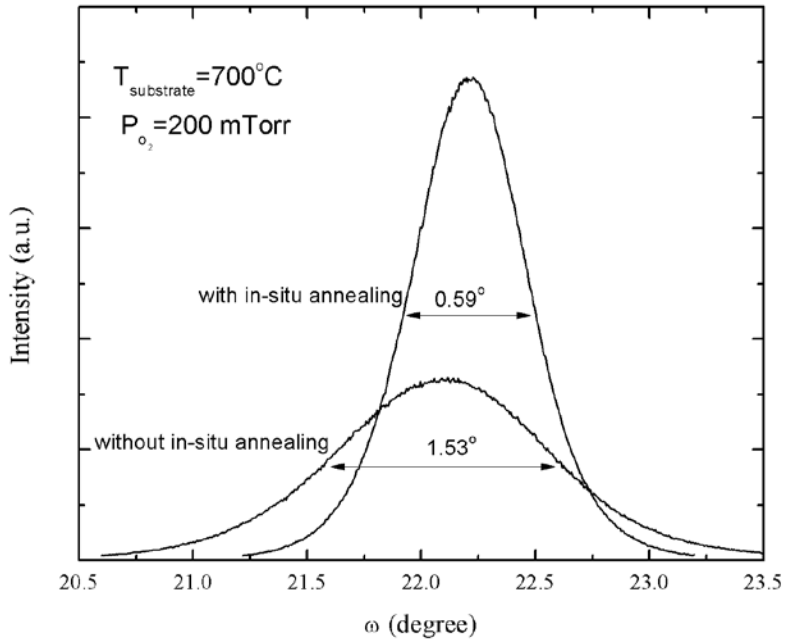

Figure 3.6. The XRD rocking curve of the BCZN film (002) peak grown at 700 ^{o}C with and without in-situ annealing

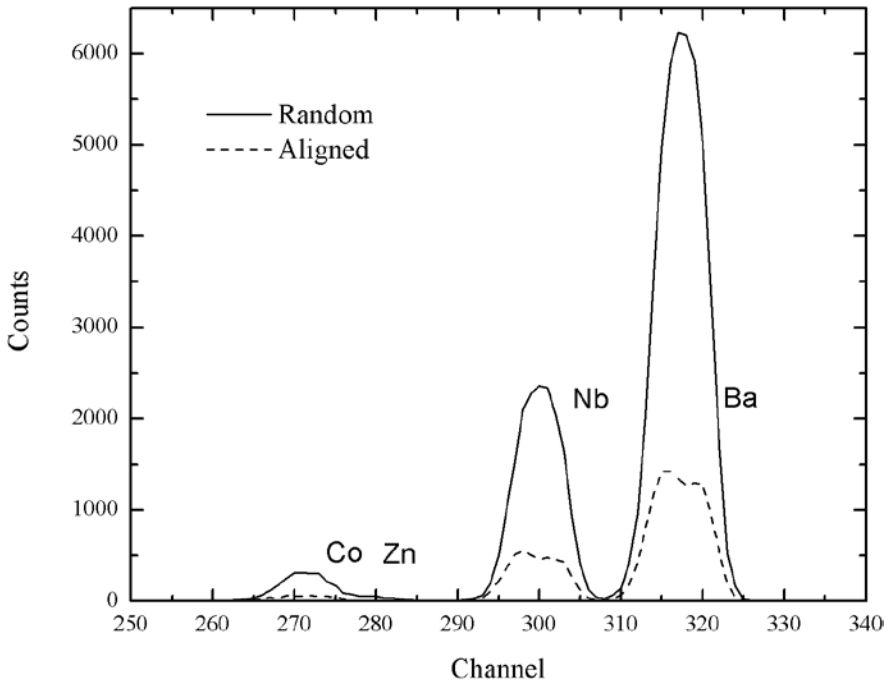

Figure 3.7. Spectrum of channeling RBS of the BCZN film grown at 700^{o}C with a thickness of 48nm, solid lines show the measurement when ion beam was away from any crystalline direction, dashed lines show the measurement when aligned to <001> crystalline direction.

RBS ion channeling has been done to check the lattice perfection and site of the atoms. The incident He^{2+} ion beam with energy of 2 MeV was carefully aligned in the <001> direction. The ratio of the yield of backscattered ion when aligned to a crystalline direction to that when not aligned is expressed as χ_{min}. RBS ion channeling has been done to check the lattice perfection and to determine the site of the atoms. The χ_{min} of Ba, Co, Zn and Nb were 21%, 19%, 18% and 21% respectively for the film grown at 700 ^{o}C as shown in Fig. 3.7 (the channel numbers are corresponding to backscattered energy used in the multichannel analyzer). The similar $\chi_{min}\approx$20% shows that nearly all the atoms are

substitutional without significant distortion [12]. The film grown at 800 ^{o}C showed an even lower χ_{min}= 8.8% at the surface, as shown in Fig. 3.8. However, the χ_{min} increased to 46% at the bottom of the film, presumably due to point and extended defects in the film acting as the scattering centers.

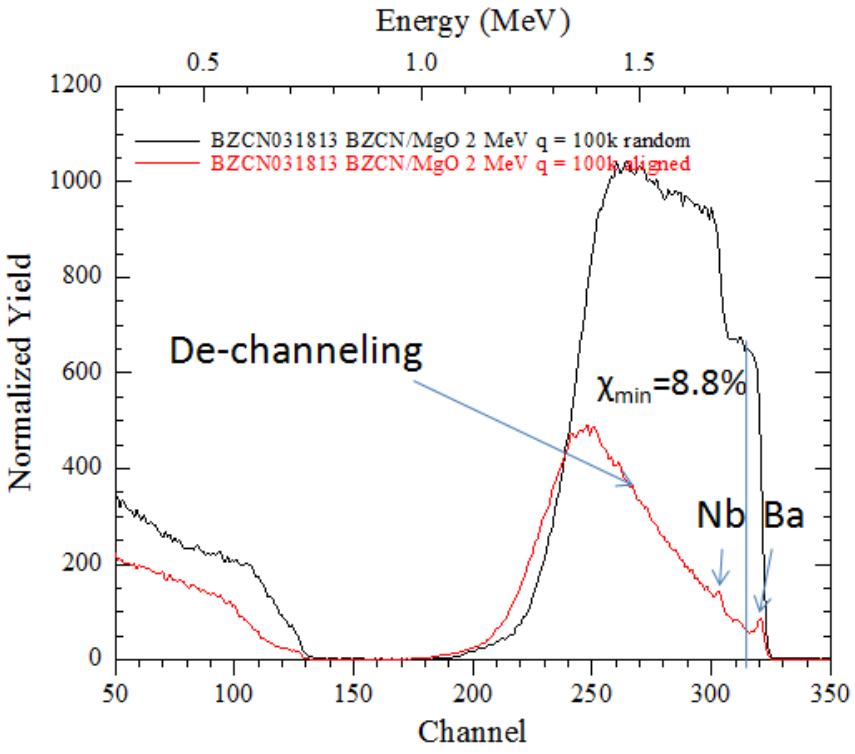

Figure 3.8. Spectrum of channeling RBS on the film grown at 800 ^{o}C with a thickness of 475 nm, black lines show the measurement when ion beam was away from any crystalline direction, red lines show the measurement when aligned to <001> crystalline direction.

The topography and roughness of the films were studied using an Atomic Force Microscope (AFM) (Digital Instrument, Dimension 3000), and the data was analyzed by

the program Veeco Nanoscope. The AFM images with areas of 1 μm×1 μm are showed in Fig. 3.9. A monotonicdecrease in the root mean square (RMS) of surface roughness with temperature is observed, as shown in Fig. 3.10. In-situ annealing was found to make the surface even smoother for the sample grown at 700 ^{o}C. Large particles observed in the AFM graph, often called "boulders" by the PLD research community, were deposited during the laser ablation process.

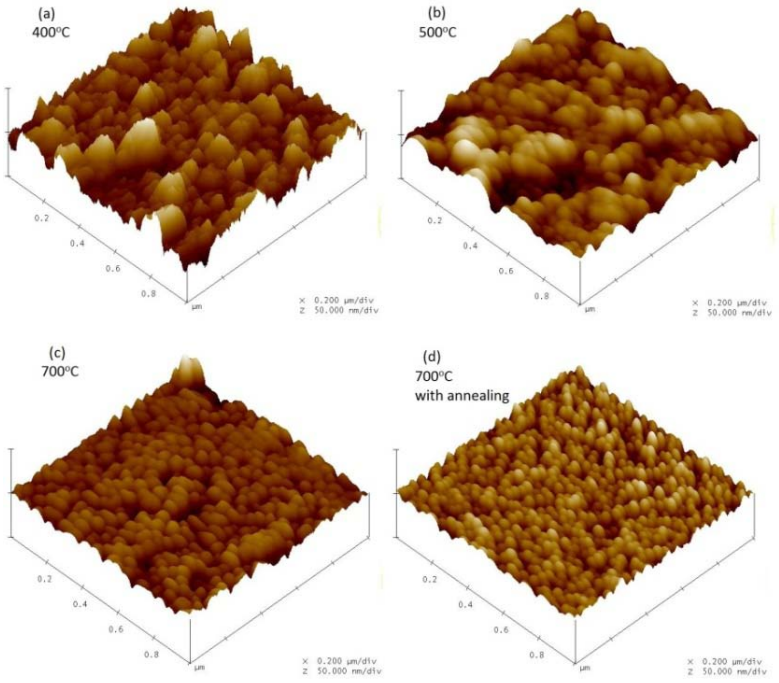

Figure 3.9 The AFM images of the BCZN thin films grown at (a) 400 ^{o}C, (b) 500 ^{o}C, (c) 700 ^{o}C without annealing, and (d) 700 ^{o}C with annealing.

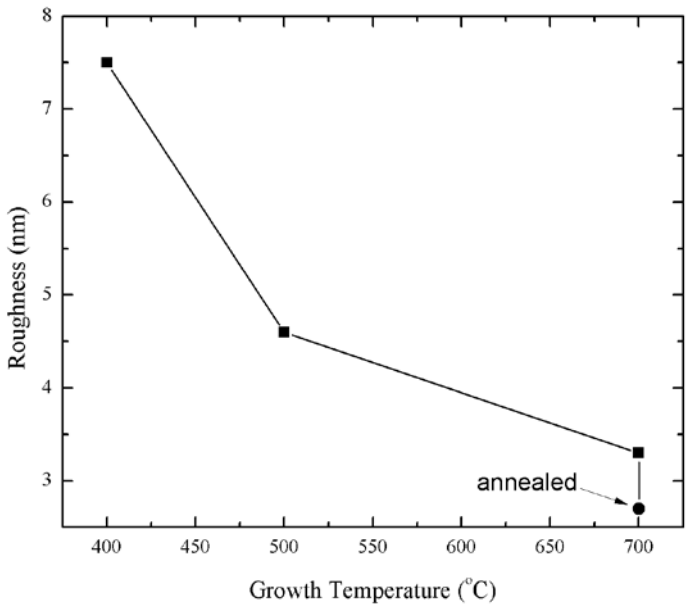

Figure 3.10. The RMS roughness of the films grown with different growth temperature and heat treatment

The optical measurement of the BCZN thin film represented in Tauc plot using the equation (2-1) with n=½ is shown in Fig. 3.11. A strong direct absorption with $\alpha>10^4$ cm^{-1} and an x-intercept at ~4.2 eV can be observed, However, according to first principle calculations by J. Yin et al. [24], the band structure of $Ba(Co_{1/3}Nb_{2/3})O_3$ (BCN) has an indirect gap with mixed Co 3d and O 2p character at the valence band maximum and Nb 4d level at the conduction band minimum. This shows strong directional covalent d-electron bonds of Co-O with enhanced phonon energy, leading to reduced microwave loss. The anticipated flat bands described in Ref. 24 would be expected to result in strong direct absorptions over most of the measured spectra and may explain why the observed linearlity in the Tauc plot of n=½, which was not found for n=2. The source of the absorption below 4.2 eV is not clear, as it could arise from indirect d to d transitions in

the partially filled Co 3d e_g levels, indirect bandgap transition from the itinerant valence band to conduction band, or transitions in localized defects with energies near the band edges in the film. Clearly further theoretical and experimental work is needed to better understand the electronic structure of this highly-correlated system.

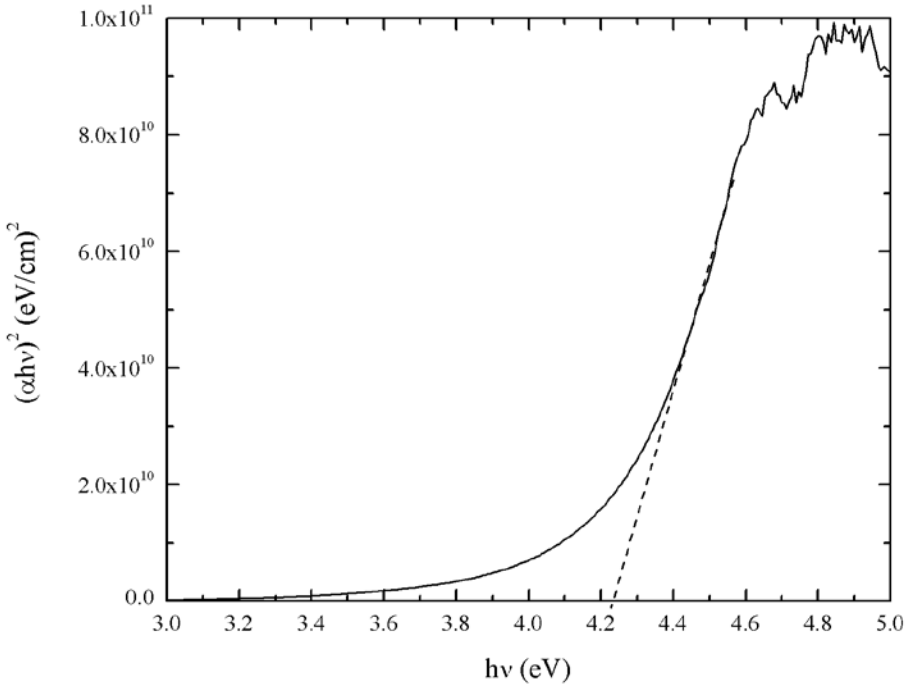

Figure 3.11 Tauc plot of optical absorption of BCZN thin film with a thickness of 450 nm grown at 500 ^{o}C on double-side polished MgO substrate. The dashed line shows the extrapolation of the linear part.

The thin film on the top of a substrate with different refractive indexes (n≈1.72 for MgO) will result in interference of reflection from the surface and the interface, arising oscillations in the transmitted light spectrum [25]. By fitting the extrema of the interference oscillation in the transmittance spectrum, shown as the dashed line in Fig. 3.11, the refractive index of thin film materials can be determined using the equation

derived by Goodman et al. [25].The refractive index is inferred to be 2.5 in the visible light range for the BCZN film. It is larger than the value of 1.9 found for the BZT film [14], and 2.1 for the BCT film [4], which is consistent with the Moss relation [26] which says that the material with smaller bandgap will have a larger refractive index.

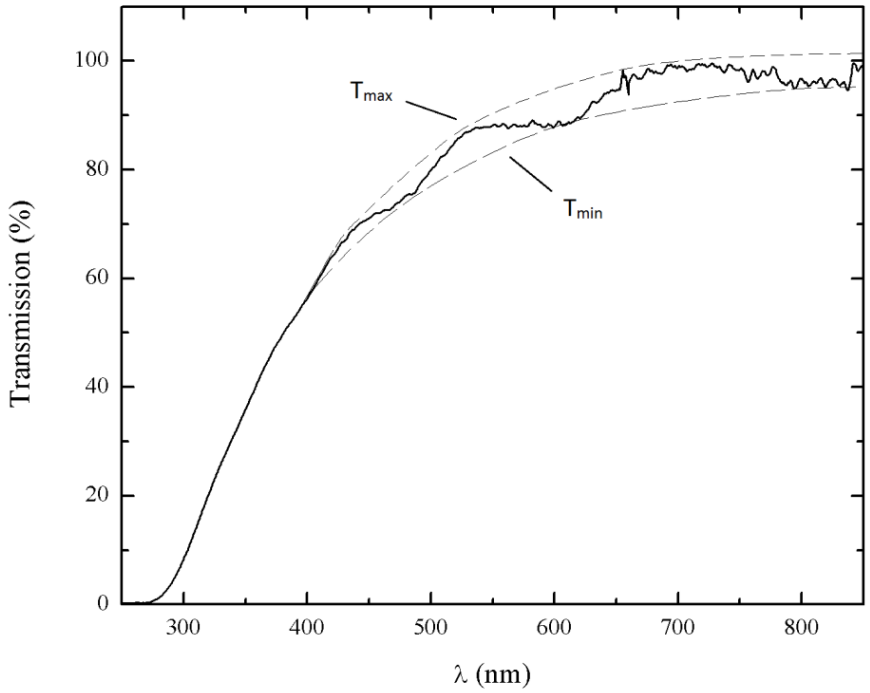

Figure 3.12. Transmission spectrum of BCZN thin film the same as that used in the absorption measurement. The dashed lines are the fitted extrema of the oscillations.

For the other substrates studied in the research, the results are summarized as below:

(1) The films on Si(100) are polycrystalline up to 700 ^{o}C, and slightly textured in (00l) directions.

(2) The films on Ge(111) show some texture but not very clear. The films don't stick to the substrate very well, especially at the region where the flux is high (close to the center of the plume), island areas form leaving some uncovered areas

(3) The films grown on $LaAlO_3$(001) are strongly textured, only showing (00l) peaks. For the sample grown at 700^{o}C, the width of the rocking curve is 2.8^{o}, which is much worse than that on the MgO substrate.

(4) The films on Al_2O_3(0001) are polycrystalline up to 500 ^{o}C.

Chapter 4

DIELECTRIC PROPERTIES MEASUREMENT OF $Ba(Co,Zn)_{1/3}Nb_{2/3}O_3$ THIN FILMS

4.1 Planar interdigital structure measurement

The electrical properties of thin films have been characterized using a planar interdigital structure. A standard lift-off technique was used to make the top electrodes as shown in the Fig 4.1. The positive photoresist AZ4330 was spin-coated on the top of the thin film and exposed by ultraviolet light under the mask, and then the Ti/Au bilayer interdigital electrodes were evaporated on the film. A standard lift-off technique was used by ultrasonic cleaning in the acetone to remove the redundant metals and finish the lithography. The interdigital structure consisted of 40 fingers that were 2 mm long and 20 μm wide and were separated by their symmetric partner by 20 μm.

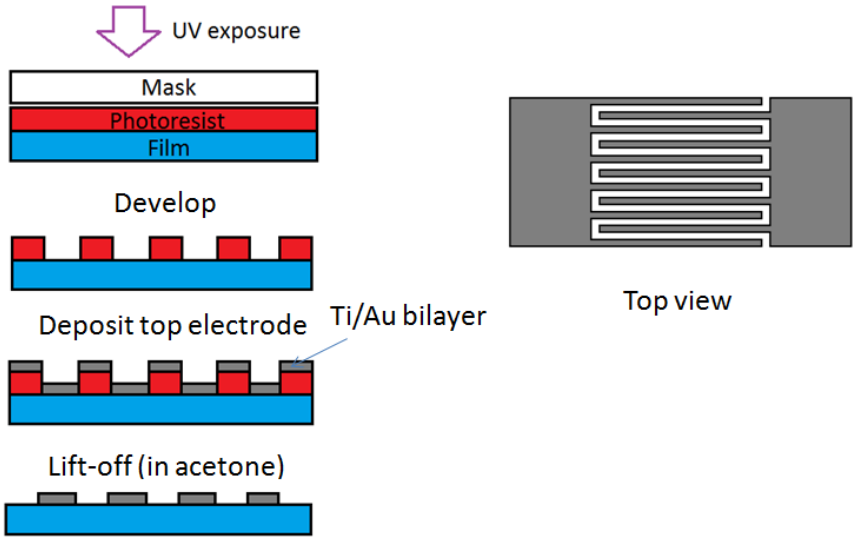

Figure 4.1. (Left) Procedures of lift-off photolithography to pattern the top electrodes; (Right) The top view of the interdigital comb structure.

A Quadtech 7400 LRC impedance meter was used to measure the capacitance of this interdigital device in a frequency range of 10 kHz ~ 1 MHz. The dielectric constant of the films could be calculated by the equations derived by Farnell et al. [27]:

$$\varepsilon_f = \varepsilon_s + \frac{C/K - (1+\varepsilon_s)}{1 - e^{-4.6h/L}} \tag{4-1}$$

$$C = \frac{C_m}{FL \times N} \tag{4-2}$$

$$N = 2P - 1 \tag{4-3}$$

Where ε_s is the dielectric constant of the substrate (9.8 for MgO), C_m is the measured capacitance, FL=2mm is the length of the finger, P is number of finger pairs, N is the number of spacing between fingers calculated by (4-3), P is the number of pairs of fingers (P=20 in this case), K=4.53 pF/m is an empirical number depending on the geometry of the interdigital structure, h is the thickness of the film, L=40 μm is the distance between the centers of adjacent fingers [28]. The measured capacitance of the device made from the 700 °C BCZN film (450 nm thick), and the dielectric constant calculated from the formula is shown in Fig. 4.2. A dielectric constant of 34 measured at frequencies from 10 kHz to 1 MHz was inferred from our measurements. As generally the dielectric constant doesn't change much up to microwave range, this value could be used for that in the microwave frequency range and it is close to the dielectric constant of 34.5 found for bulk ceramics measured at ~2.5 GHz, showing that dielectric constant of the epitaxy doesn't change relative to the polycrystal in the BCZN system.

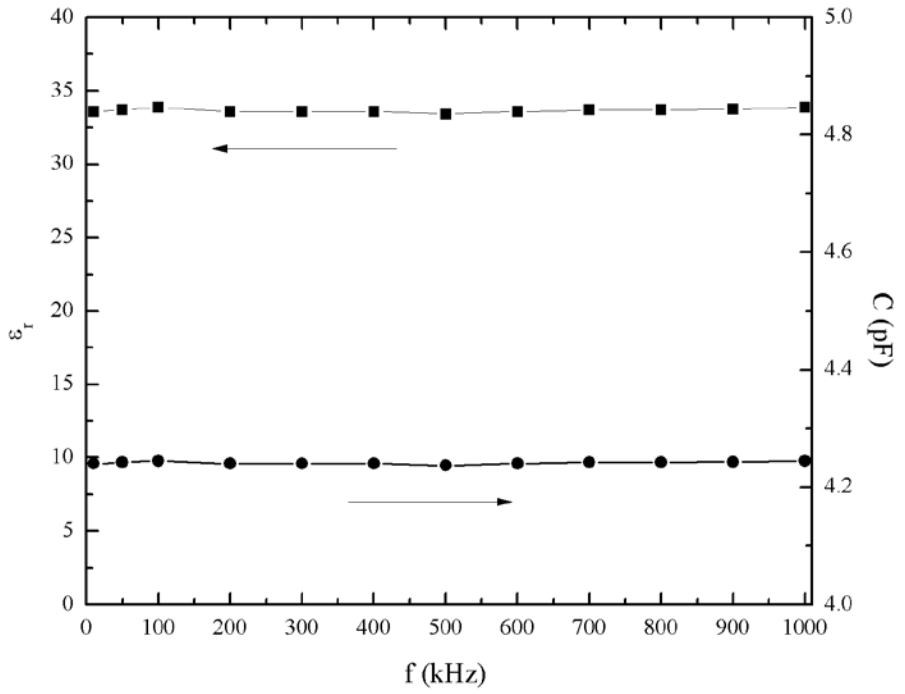

Figure 4.2 Capacitance measured at frequency from 10 kHz to 1 MHz using planar interdigital structure on the film grown at 700 ^{o}C. The dielectric constant was calculated as ~34.

The conductance-temperature (G–T) property was measured by a picoammeter (QuadTech 1865 Megohmmeter/IR tester, Maynard, MD) with a box furnace (Barnstead Thermolyne 47900). The linear relationship in the I-V measurement of patterned BCZN films grown at 700 ^{o}C showed ohmic conduction at electric field of 50 kV/cm (Bias=100 V). The log(G)–1/T Arrhenius relationship was plotted in Fig. 4.3 inferred from the transport currents $I=I_0 \exp(-E_a/kT)$ measured at temperatures between 100 and 200 ^{o}C. A thermal activation energy E_a was determined as ~0.66 eV by the slope. The resistivity of this film was inferred to be ~3×10^{10} Ω·cm at room temperature.

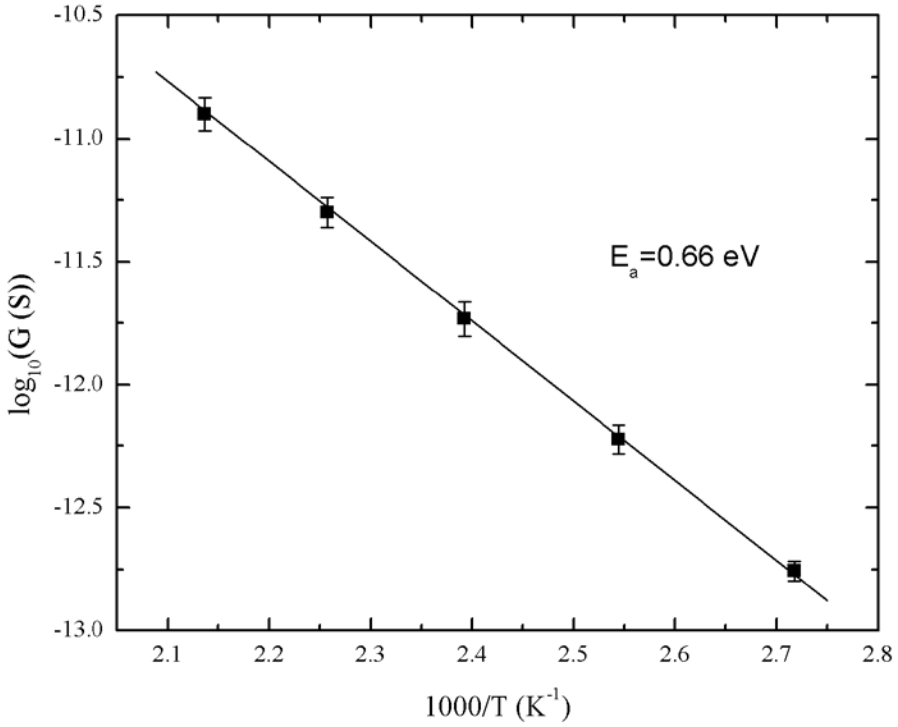

Figure 4.3 Arrhenius plot of conductance at a field of 50 kV/cm in the BCZN thin film grown at 700 ^{o}C, the thermal activation energy is determined as E_a=0.66 eV

4.2 Parallel Plate Resonator (PPR)

The parallel plate resonator used in the research is a dielectric material sandwiched in two parallel superconducting films. The overall unloaded Q of the resonator is given by [17]:

$$Q^{-1}=\tan\delta + \alpha s + \beta R_s/s \qquad (4\text{-}4)$$

where s is the spacing between conductors, a and β are coefficients that depend on geometry and frequency. The first term comes from the dielectric loss tan δ from the dielectric spacer, which is independent of spacing. The second term is the near-field energy radiation from the surrounding of the resonator (radiation loss), and it will increase linearly with the spacing. The third term is the contribution from R_s will vary as

the reciprocal of the spacing. α and β are the associated coefficients: $\beta=1/(\pi\mu)=3.9\times10^{-5}$ m/Ω at 6.5 GHz, and α is different from sample to sample. If the spacing and R_s can be made small enough, the resonator Q will become a direct measure of the loss tangent of the dielectric material in between.

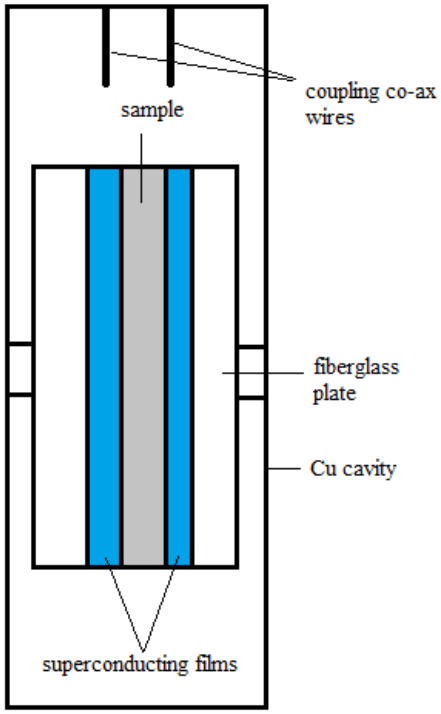

Figure 4.4. Structure of the parallel plate resonator

The sample is sandwiched between two superconducting Nb films (1 cm^2) deposited on Yttrium stabilized Zirconia (YSZ) substrates fabricated with sputter deposition (MIT Lincoln lab), with a low surface resistance of ~12 μΩ at 4.2 K scaled to 6.5GHz, then amounted with two fiber glass plate inside a gold-plated copper RF cavity (gold plating purity > 99.9%, 8 to 13 μm thick, Gold Tech Industries, Tempe, AZ). The cavity size is 20.3 mm×6.1 mm×15.2 mm, with two semirigid co-ax wires hanging in it.

It is then affixed to the end of a cryogenic dipping probe. Then the cavity is dipped into a liquid helium dewar at 4.2 K. The low temperature transmission S_{21} parameter measurements is carried out by a HP8510 microwave vector network analyzer (VNA), which could excite fundamental electromagnetic and higher resonance modes and record the associated S_{21} vector values. These values are fit to a circle in the Smith chart to infer the quality factor. The distance between coupling loops and sample is adjusted to be weakly coupled so that the unloaded Q can be determined to better than a few percent. In order to remove the silver paste on the back of the substrate used during the growth, a 30% ammonia hydroxide and 30% hydrogen peroxide were mixed in 1:1 volume ratio, then using a Q-tip to dip in the solution and take out to wipe and clean the back surface of the sample, until all the white silver were dissolved.

Actually the electromagnetic fields go through the substrate and the film simultaneously. Assuming that the concentration of the field is proportional to the layer thickness as well as the dielectric constant, the total Q of the resonator can be approximated as

$$Q_{Total}^{-1} = \frac{d_{sub}\,\varepsilon_{sub}}{d_{film}\,\varepsilon_{film} + d_{sub}\,\varepsilon_{sub}} Q_{sub}^{-1} + \frac{d_{film}\,\varepsilon_{film}}{d_{film}\,\varepsilon_{film} + d_{sub}\,\varepsilon_{sub}} Q_{film}^{-1} \qquad (4\text{-}5)$$

as the $d_{film}\,\varepsilon_{film} \gg d_{sub}\,\varepsilon_{sub}$, the above equation can be simplified as

$$Q_{Total}^{-1} = Q_{sub}^{-1} + \frac{d_{film}\,\varepsilon_{film}}{d_{sub}\,\varepsilon_{sub}} Q_{film}^{-1} \qquad (4\text{-}6)$$

In this way, we can calculate the Q of the thin film from the Q measured from the PPR measurement. The MgO substrate with a thickness of 500 μm has Q_0=115.7k at f_0= 7.48 GHz, and scaled to 6.5GHz Q_0=133k. Thick film were grown with thickness 1-3μm, the measured Qs are shown in table 4-1.

Table 4-1 Calculated Q of thin films grown at different temperatures as measured by PPR

T_s (^oC)	Thickness (nm)	Q (scaled to 6.5 GHz)
500	2899	2035
600	2319	621
700	1261	711
800	956	139

The calculated Qs seem to be not related to the film quality. However, this conclusion may not be correct because the distribution of the electromagnetic fields in the materials is not well calculated. The equation (4-6) should be modified to better describe the distribution of the electromagnetic fields in the sample. Moreover, the measured Q is very sensitive to the position of the sample in the cavity, and can be affected by other factors like the little amount residue silver paste on the back. It is also possible that the film thickness is too small relative to the substrate (500μm), so that the Q_{film} may not even affect the $Q_{Total.}$ More sophisticated analysis should be done to measure the Q_{film} by the PPR technique.

Chapter 5

SUMMARY AND FUTURE WORK

5.1 Summary

Two commonly used dielectric materials, $ZrTiO_4$-$ZnNb_2O_6$ (ZTZN) and $Ba(Co,Zn)_{1/3}Nb_{2/3}O_3$ (BCZN), have been grown with PLD with different growth conditions. Very good film quality has been achieved at elevated temperature.

ZTZN films were grown on Si with randomly oriented polycrystalline structure when the temperature is above 700 ^oC. It grows textured on MgO at 700 ^oC. The 4-fold symmetry showed in the XRD asymmetry φ scan indicates that the lattice changed from orthorhombic to tetragonal.

BCZN films were grown on MgO(100), Si(100), Ge(111), $LaAlO_3$(100) and Al_2O_3(0001). Good epitaxial growth was only achieved on MgO substrate above 500 ^oC by PLD, with (001)//MgO(001) and (100)//MgO(100). The compositions don't change much up to 800 ^oC. In-situ annealing at the same growth temperature in 200 mTorr oxygen pressure can be used to enhance the quality of the film, reducing the peak width of the XRD rocking curve from 1.53^o to 0.59^o for the film grown at 700 ^oC. The film grown at 800 ^oC had the best structural quality, with a XRD rocking curve width of 0.53^o and χ_{min} of channeling Rutherford Backscattering Spectrometry of 8.8%. AFM measurements were used to measure the topography and found a monotonic decrease in the RMS of surface roughness to ~3 nm for films deposited at 700 ^oC. Optical transmission measurements indicate a strong direct transition at ~4.2 eV. The refractive index of BCZN was inferred to be 2.5 in the visible light range. Temperature-dependent

electrical measurements have determined a room temperature resistivity of $3\times10^{10}\,\Omega\cdot$cm with a thermal activation energy of ~0.66 eV. A low-frequency dielectric constant of 34 was measured at room temperature. Dielectric measurement at microwave frequency was carried out using the PPR technique, but no obvious relationship between the film quality and the loss tangent was observed.

The excellent structural, optical and electrical properties, the relatively cheap cost, and the potential to enable a marked reduction in the size of communication devices and systems, make the thin films of high performance dielectrics like ZTZN and BCZN promising candidates for use in a number of microelectronic and microwave communication applications.

5.2 Future Work

Channeling RBS angular distribution of the film in different crystalline directions could be done to further determine the specific sites of the elements in epitaxial BCZN film. The energy band structure of BCZN could be carefully analyzed by local density analysis (LDA) and measured with optical diffuse reflection or cathodoluminescence.

For the dielectric measurement, we could use the program HFSS (Ansys) to calculate the distribution of the electric field by finite element method, so that the contribution from the film and the substrate to the dielectric loss can be separated. Additionally, the Q of the films could be measured by coplanar waveguide (CPW), which constrains the electromagnetic fields only in the films. Conduction loss from the electrodes should be considered and subtracted, and then the Q from the film can be accurately determined [29].

REFERENCES

[1] I. M. Reaneyw, D. Iddles, J. Am. Ceram. Soc., **89** [7] 2063–2072 (2006).

[2] D. Cruickshank, *Microwave Materials for Wireless Applications*, 2011.

[3] D. Cruickshank, Journal of the European Ceramic Society **23** (2003) 2721–2726.

[4] L.T. Liu, C. Kopas, R.K. Singh, R.M. Hanley, N. Newman, Thin Solid Films **520** (2012) 6153–6157.

[5] L.T. Liu et al., "Resonance techniques to accurately measure the loss tangent and EPR spectrum of small dielectric samples", in manuscript.

[6] L.T. Liu, M. Flores, and N. Newman, Phys. Rev. Lett. **109**, 257601 (2012).

[7] O. Nakagawara et al., J. Appl. Phys. **80** (1), 1 July 1996.

[8] Y Kim et al., Jpn. J. Appl. Phy. Vol. **40** (2001) pp. 4599-4603.

[9] KAWASHIMA, S., NISHIDA, M., UEDA, I. and OUCHI, H. Journal of the American Ceramic Society, **66** (1983) 421–423.

[10] M. Ohring, *Materials Science of Thin Films*, 2nd edition, 2002.

[11] Zhizhong Tang, PhD dissertation, 2010.

[12] T. Alford, *Fundamentals of Nanoscale Film Analysis*, 2007.

[13] en.wikipedia.org/wiki/Electron_paramagnetic_resonance, Retrieved on 4.16.2013.

[14] Z.Z. Tang, Acta Materialia **57** (2009) 432–440.

[15] M Nistor, A Ioachim, B Gallas, D Defourneau, J Perriere and W Seiler, J. Phys.: Condens. Matter **19** (2007) 096006 (16pp).

[16] J. Tauc et al., Mater. Res. Bull. **3** (1968) 37.

[17] R. C. Taber, Rev. Sci. Instrum. **61**, 2200 (1990).

[18] N. A. Shtin, F.M.L.Romero and E. Prokhorov, *J. Appl. Phys.* **106**, 104115 (2009).

[19] Bhalla AS, Guo R, Roy R. Mat Res Innovat (2000) 4:3.

[20] M. Hill, D. Cruickshank ACERS AMA. 1-A-01-2002, April 2002.

[21] Ahn, Cheol-Woo; Nahm, Sahn; Yoon, Seok-Jin; Park, Hyun-Min; Lee, Hwack-Joo, Japanese Journal of Applied Physics, Volume **42**, Issue 11, pp. 6964 (2003).

[22] I. M. Reaney, E. L. Colla and N. Setter, Jpn. J. Appl. Phys. **33** (1994) pp. 3984-3990.

[23] J.Y. Tsao, Materials Fundamentals of Molecular Beam Epitaxy, Academic Press,New York NY, 1993.

[24] J. Yin, Z. Zou, and J. Ye, J. Phys. Chem. B 2003, **107**, 4936-4941.

[25] A.M. Goodman, Appl. Optics **17** (1978) 2779.

[26] N.M. Ravindra, P. Ganapathy, J. Choi, Infrared Phys. Technol. **50** (2007) 21.

[27] G.W. Farnell, I.A. Cermak, P. Silvester, S.K.Wong, IEEE Trans. Sonics Ultrason. SU-**17** (1970) 188.

[28] D. Dimos, M.V. Raymond, R.W. Schwartz, H.N. Al-Shareef, C.H. Mueller, J. Electroceram. **1** (1997) 145.

[29] Z. Ma et al., IEEE TRANSACTIONS ON ELECTRON DEVICES, VOL. **45**, NO. 8, AUGUST 1998

[30] B. Bishnoia, P.K. Mehtaa, C.J. Panchalb, M.S. Desaib, R. Kumarc, V. Ganesand, Materials Chemistry and Physics **126** (2011) 660–664.